HHS Public Access

Author manuscript

Cell Rep. Author manuscript; available in PMC 2021 January 16.

Published in final edited form as:

Cell Rep. 2020 December 08; 33(10): 108482. doi:10.1016/j.celrep.2020.108482.

Regulatory T Cells Support Breast Cancer Progression by Opposing IFN-γ-Dependent Functional Reprogramming of Myeloid Cells

Nicholas M. Clark[1,2], **Leandro M. Martinez**[1], **Steven Murdock**[1], **James T. deLigio**[1], **Amy L. Olex**[3], **Comfort Effi**[1], **Mikhail G. Dozmorov**[4,5], **Paula D. Bos**[1,5,6,*]

[1]Department of Pathology, Virginia Commonwealth University School of Medicine, Richmond, VA 23298, USA

[2]Integrative Life Sciences Graduate Program, Virginia Commonwealth University, Richmond, VA 23298, USA

[3]C. Kenneth and Dianne Wright Center for Clinical and Translational Research, Virginia Commonwealth University, Richmond, VA 23298, USA

[4]Department of Biostatistics, Virginia Commonwealth University, Richmond, VA 23298, USA

[5]Massey Cancer Center, Virginia Commonwealth University School of Medicine, Richmond, VA 23298, USA

[6]Lead Contact

SUMMARY

Regulatory T (Treg) cell infiltration of solid tumors often correlates with poor prognosis, but their tumor-suppressive function lacks mechanistic understanding. Through a combination of transgenic mice, cell fate mapping, adoptive transfer, and co-injection strategies, we demonstrate that Treg cell ablation-dependent antitumor effects in murine breast cancer require intratumoral recruitment of $CCR2^{+}$ inflammatory monocytes, which primarily differentiate into tumor-associated macrophages (TAMs), and lead to reprogramming of their function in an IFN-γ-dependent manner. Furthermore, transcriptomic signatures from murine TAMs in Treg cell-ablated conditions correlate with increased overall survival in human breast cancer. Our studies highlight the strong myeloid dependency of breast cancer and provide the basis for the development of therapeutic strategies based on manipulation of the IFN-γ signaling pathway in monocytes.

In Brief

*Correspondence: paula.bos@vcuhealth.org.

AUTHOR CONTRIBUTIONS

N.M.C. and P.D.B. designed the project, analyzed the experiments, and wrote the manuscript. N.M.C. and L.M.M. performed most of the experiments, with assistance from S.M. C.E. performed the immunohistochemistry analysis. J.T.D. performed the $CD4^{+}$ T cell transfer experiments. M.G.D. performed all of the RNA sequencing pre-processing. A.L.O. performed the bioinformatics analysis of the human datasets. P.D.B. supervised all aspects of the project. All of the authors read and commented on the manuscript.

DECLARATION OF INTERESTS

The authors declare no competing interests.

SUPPLEMENTAL INFORMATION

Supplemental Information can be found online at https://doi.org/10.1016/j.celrep.2020.108482.

Treg cells correlate with poor prognosis in breast cancer, yet we lack mechanistic insights on how they promote tumorigenesis. Clark et al. demonstrate that anti-tumor effects following Treg cell ablation in murine breast tumors require IFN-γ-dependent functional reprogramming of inflammatory monocytes/TAMs and correlate with prognosis in human breast cancer.

Graphical Abstract

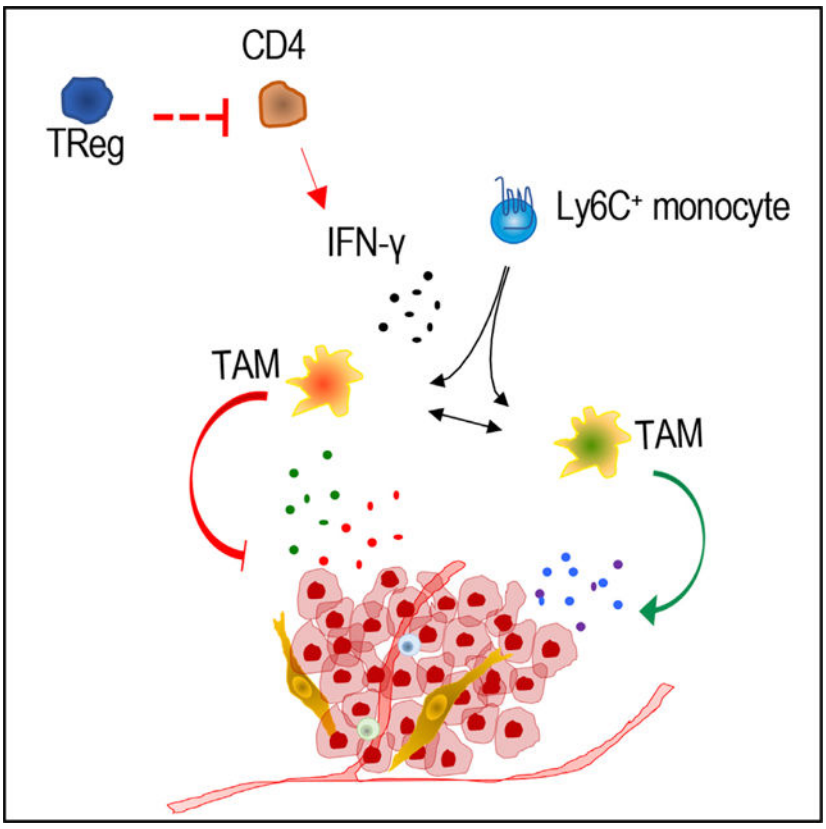

INTRODUCTION

Breast cancer is the most prevalent cancer in women worldwide, and it is characterized by a low mutational load compared to other tumors (Alexandrov et al., 2013). While tumor infiltrating lymphocytes (TILs), including regulatory T (Treg) cells, seem to be prognostic in triple negative breast cancers (TNBCs), their predictive value in estrogen receptor-positive (ER^+) breast cancer is less clear (Vonderheide et al., 2017). Moreover, results from immune checkpoint blockade (ICB) immunotherapy have been only modest as compared to other cancers such as melanoma and non-small lung cell cancer (Luen et al., 2016; Nolan et al., 2017). This is particularly true for ER^+ tumors, considered to be less immunogenic (Denkert, 2014; Miller et al., 2016; Nagalla et al., 2013). Therefore, a deeper understanding of the immunobiology of breast cancer is critical to the success in harnessing immunotherapeutic approaches to improve breast cancer patient survival.

Treg cells are characterized by the expression of the transcription factor Foxp3 and evolved to protect the organism from immune responses to self-antigens (Josefowicz et al., 2012). This suppressive function is also responsible for restraining anti-tumor immunity (Tanaka and Sakaguchi, 2017). Experimental targeting of Treg cells using depleting antibodies or genetic ablation in several tumor models results in growth inhibition. However, their suppressive mechanisms depend on the tumor type studied, with CD8 T or natural killer (NK) cell cytolytic activities being the predominant way in which effector anti-tumor functions manifest (Bos et al., 2013; Jang et al., 2017; Joshi et al., 2015; Klages et al., 2010; Li et al., 2010; Shimizu et al., 1999; Teng et al., 2010). Using a mouse model of breast cancer genetically driven by the expression of the polyoma middle T antigen in mammary epithelial cells (MMTV-PyMT) and molecularly characterized as ER^+, luminal B subtype (Herschkowitz et al., 2007), we have previously established that transient ablation of Treg cells resulted in a significant reduction in primary and lung metastatic growth, with an associated increase in apoptotic tumor cell death (Bos et al., 2013). Importantly, using a cell line derived from those tumors that is refractory to current ICB, antibody depletion and genetic analysis demonstrated that unlike other models, this anti-tumor effect in mammary carcinomas is independent of cytotoxic $CD8^+$ T and NK cell responses. Conversely, anti-tumor activities required both $CD4^+$ T cells and interferon gamma (IFN-γ) (Bos et al., 2013).

Tumor-associated macrophages (TAMs) are one of the most abundant leukocytic populations in breast cancer (Noy and Pollard, 2014), and they are critical regulators of tumor progression, metastatic dissemination, and therapeutic resistance (Qian and Pollard, 2010; Ruffell and Coussens, 2015). Macrophages are extremely sensitive to their microenvironment, readily adapting to changing environmental factors and acquiring different properties. They take on a number of intermediate phenotypes ranging from classically activated (M1) macrophages that promote inflammation and oppose tumor growth to alternatively activated (M2) macrophages, associated with tissue repair mechanisms and tumor-supporting functions (Ruffell et al., 2012; Azizi et al., 2018). IFN-γ is a potent anti-tumor cytokine itself, but it is also responsible for the classical activation of macrophages, resulting in increased pro-inflammatory and tumoricidal functions, antigen-presenting capacity, and induction of cytotoxic T cell activity (Dunn et al., 2005; Alspach et al., 2018). Analysis of tumors formed upon the orthotopic injection of MMTV-PyMT-derived tumor cells (PyMT) in Treg cell ablated mice revealed a strong upregulation of IFN-γ on the T cell compartment and its targets (e.g., CXCL9, CXCL10, iNOS) in the myeloid compartment (Bos et al., 2013). Therefore, we investigated the hypothesis that the critical function of Treg cells in breast cancer is to suppress IFN-γ-dependent activation of monocyte/TAMs, preventing their anti-tumor function, therefore facilitating tumor progression.

In the present work, we mechanistically dissect the tumor-promoting function of Treg cells in poorly immunogenic breast cancer, describing the critical role of TAMs in the anti-tumor phenotype observed upon Treg cell ablation, and the dependency on $CD4^+$ T cell-produced IFN-γ for their functional reprogramming. Furthermore, we demonstrate that human cancers with gene expression patterns similar to those elicited by Treg cell ablation within mouse

TAMs correlate with better overall survival, highlighting the clinical relevance of our findings.

RESULTS

Treg Cell Ablation-Driven Anti-tumor Effects Depend on CCR2-Mediated Recruitment of Bone Marrow Cells

Mammary gland macrophages in *MMTV-PyMT* and other breast cancer models analyzed originate from Ly6C^{hi}CCR2^{+} bone marrow monocytes (Franklin et al., 2014; Tymoszuk et al., 2014). Moreover, a large proportion of the CD45^{+}CD11B^{+} F8/ 40^{+} macrophage population in orthotopically implanted PyMT tumors growing in *Ccr2^{GFP}* reporter mice still expresses the CCR2 reporter gene (Figures S1A and S1B), suggesting that targeting the CCR2 pathway may be a good strategy to address their requirement downstream of Treg cell ablation. Therefore, we crossed *Foxp3^{DTR}* mice to *Ccr2^{DTR}* depleter mice (Hohl et al., 2009), where injection of diphtheria toxin (DT) abolishes CCR2 receptor-expressing cells at the same time that it eliminates Treg cells, eliminating the population of bone-marrowderived inflammatory monocytes in the tumor. Challenge of these mice with the same DT regimen optimized to ablate Foxp3^{+} Treg cells (Bos et al., 2013), in which DT is injected at a dose of 50 mg/kg on 2 consecutive days (Figure 1A) achieved transient but effective elimination of CCR2^{+} cells in the tumor microenvironment, with near-complete loss for the first 2 days (Figures S1C and S1D). Importantly, this transient deletion of CCR2^{+} cells alone proved inconsequential to primary tumor growth in the orthotopic tumor model, as evaluated by tumor growth kinetics and primary tumor weight at necropsy (Figures S1E and S1F). Of note, the presence of the *Ccr2^{DTR}* transgene has no effect on tumor growth kinetics in untreated mice (Figures S1G and S1H). Remarkably, co-ablation of Treg cells and CCR2^{+} cells completely abolished the anti-tumor effect caused by Treg cell ablation alone in PyMT primary tumors, as demonstrated by the similar primary tumor growth kinetics and final weight in the double-ablated and control groups (Figures 1B and 1C). To investigate whether this observation can be extended to other syngeneic breast cancer models, we performed orthotopic transplantation studies using the EO771 cell line (CH3 Biosystems). This cell line was originally established from a spontaneous tumor growing in the mammary gland of a C57BL/6 mouse and was characterized by the positive expression of hormone receptors (Ewens et al., 2005; Sugiura and Stock, 1952). We found that EO771 orthotopic growth in the mammary glands of *Foxp3^{DTR}* mice was also very sensitive to Treg cell ablation, with primary tumor growth kinetics, final weight, and lung metastatic burden being significantly reduced upon the transient targeting of Treg cells (Figures S2A–S2C). Importantly, this anti-tumor effect was significantly impaired when targeting CCR2^{+} cells simultaneously with Treg cells in the *Foxp3^{DTR} Ccr2^{DTR}* double-depleter mice (Figures 1D and 1E), suggesting a general role of bone-marrow-derived cells in mediating Treg cell pro-tumorigenic activities. Interestingly, we noticed that this acute and short ablation of CCR2^{+} cells only marginally restores lung metastatic burden in DT-treated PyMT and EO771 tumor-bearing mice, hinting at different biological mechanisms taking place at the metastatic site (Figures 1F and 1G, respectively). These results suggest that the critical effector cell type downstream of Treg cell ablation in primary tumors is recruited from the bone marrow compartment via the CCR2 pathway.

Ablation of Treg Cells Does Not Alter the Proportion of CCR2$^+$ Recruited Cells, but Their Phenotypes

The CCL2/CCR2 chemokine axis is essential for the recruitment of inflammatory monocytes to sites of inflammation (Shi and Pamer, 2011). However, other bone marrow cells have been shown to migrate to the tumor via CCR2, such as mesenchymal cells or gamma delta T cells (Lanç a et al., 2013; Dwyer et al., 2007). To investigate the fate of these CCR2$^+$ cells in breast tumors and determine whether the presence of Treg cells contributes to a differential recruitment or differentiation of various cells, we performed a fate mapping experiment using *Ccr2^{GFP} Foxp3^{DTR}* double transgenic mice (Hohl et al., 2009). We allowed PyMT and EO771 tumors to become established to an approximate size of 100 mm^3, ablated Treg cells with the same DT regimen as before, and analyzed the tumors 4 days after this intervention (Figures 2A and S2D–S2F). Analysis of CCR2$^+$ cells recruited to the primary tumor from the circulation revealed a predominance of myeloid cells, in particular inflammatory monocytes and macrophages. Importantly, the relative frequency of the different tumor-infiltrating cell populations was not influenced by the presence of Treg cells, with only a slight, although not significant, decrease in the frequency of TAMs observed upon Treg cell ablation in EO771-derived tumors (Figures 2B, 2C, S2E, and S2F). To confirm that the number of TAMs was not affected by Treg cell ablation, we quantified CD45$^+$CD11B$^+$ Ly6G$^-$ F4/80$^+$ macrophages in control and DT-treated PyMT and EO771 tumors by flow cytometry (Figures 2D and 2E, respectively) and did not observe significant differences. Furthermore, we also found a similar number of Iba-1$^+$ cells in fixed tumor tissues of both tumor types by immunofluorescence analysis (Figures 2F and 2G). However, fluorescence-activated cell sorting (FACS) analysis of the CD45$^+$CD11B$^+$ Ly6G$^-$ F4/80$^+$ population revealed the upregulation of MHCII, CD80, and CD86 in tumors from DT-treated mice (Figures 2H–2J). Combined, these data suggest that it is a functional switch consistent with a more classically activated TAM phenotype, and not a change in absolute numbers, that mediates the anti-tumor effect observed after Treg cell ablation.

CCR2$^+$Bone-Marrow-Derived Ly6C$^+$Monocytes Are Key Mediators of the Anti-tumor Effect of Treg Cell Ablation

Our analysis of tumor-infiltrating cells confirmed that there was a small but significant contribution of cells other than monocytes and macrophages to the CCR2$^+$ pool, including non-hematopoietic and non-myeloid cell types. This raises the possibility that multiple effector cell types from the bone marrow may play a role in the anti-tumor phenotype following Treg cell ablation. To address this issue, we performed a rescue experiment in which we adoptively transferred CCR2$^+$ CD11B$^+$ Ly6C$^+$ Ly6G$^-$ inflammatory monocytes from the bone marrow of tumorbearing *Ccr2^{GFP}* reporter mice intravenously into tumor-bearing *Foxp3^{DTR} Ccr2^{DTR}* mice 6 h after the Treg cell/CCR2 double-cell ablation (Figure 3A and 3B). Notably, this transfer strategy significantly rescued the anti-tumor phenotype in both the PyMT and the EO771 tumor models (Figures 3C–3H), implicating Ly6C$^+$ inflammatory monocyte as the critical source for the intratumoral effector cell type responsible for the Treg cell ablation-triggered anti-tumor activity. Furthermore, using the same fate-mapping strategy described previously, we analyzed the identity of the transferred CCR2$^+$ monocytes in the tumors of the rescued mice 72 h after the adoptive transfer (Figure S3A). We observed that ~80% of the CCR2$^+$ CD11B$^+$ cells we found in the tumors gave rise

to F4/80$^+$ TAMs, followed by a very small proportion of monocytic dendritic cells (CD11B$^+$ F4/80$^-$ CD11C$^+$), myeloid suppressor cells (CD11B$^+$ F4/80$^-$ Ly6C$^+$ Ly6G$^+$), inflammatory monocytes (CD11B$^+$ F4/80$^-$ Ly6C$^+$ Ly6G$^-$), and neutrophils (CD11B$^+$ F4/80$^-$ Ly6C$^-$ Ly6G$^+$) (Figures S3B and S3C). These data indicate that inflammatory monocyte-derived TAMs are critical for the anti-tumor phenotype observed upon Treg cell ablation.

Treg Cell Ablation Induces a Functional Reprogramming of TAMs

Next, we decided to directly test the role of TAMs in the phenotype observed upon Treg cell ablation. To this end, we FACS sorted tumor-infiltrating CD11B$^+$ F4/80$^+$ Ly6G$^-$ cells from dissociated control and Treg cell-ablated PyMT and EO771 tumors 4 days after DT treatment, as we previously described (Clark and Bos, 2019) (Figure 4A). We performed orthotopic co-injections of sorted TAMs and tumor cells in equal ratios into the mammary glands of virgin female NOD *scid* gamma receptor null (NSG) mice (Figure 4A). NSG hosts, lacking adaptive immunity and with compromised innate immunity, were chosen to provide an environment possibly more sensitive to modulatory effects originating from the transplanted TAMs. Interestingly, both PyMT and EO771 tumor cells demonstrated a significant delay in primary tumor growth when co-injected with TAMs obtained from Treg cell-ablated versus control tumors (Figures 4B and 4F), resulting in smaller tumors at the end of the experiment (Figures 4C and 4G). When we performed histological analysis on these endpoint tumors, we observed an increase in apoptotic tumor cell death, as evaluated by the quantification of cleaved-caspase 3 staining (Figures 4D and 4H), with a dense infiltration of F4/80$^+$ cells in the apoptotic areas (Figure S4C). Correspondingly, lung tumor burden was also significantly decreased in the groups of mice co-injected with TAMs from Treg cell-ablated tumors (Figures 4E and 4I). To further extend our findings, we obtained a third syngeneic murine breast cancer cell line generated by tumor dissociation from p53/KrasG12D/myristoylated p110α (BRPKP110) transgenic mice, and characterized as hormone sensitive (Rutkowski et al., 2015). As with all breast cancer models tested thus far, BRPKP110 cells also responded to Treg cell ablation by exhibiting a very significant inhibition of primary tumor growth (Figures S4A and S4B), although undetectable metastasis to the lungs in control mice, as reported in the literature, prevented us from evaluating the consequence of this intervention on systemic disease. Importantly, co-injection of BRPKP110 cells with sorted TAMs followed the same pattern observed previously, with TAMs from the Treg cell-ablated tumors hindering tumor growth (Figures 4D and 4E). We further investigated this TAM functional reprogramming in spontaneously developing tumors, in which more complex microenvironmental interactions may be taking place. To this end, we isolated TAMs from *MMTV-PyMT Foxp3^{DTR}* tumors ranging in size from 100 to 900 mm^3 under control or Treg cell ablated conditions, and co-injected them with dissociated tumor cell suspensions prepared from advanced MMTV-PyMT tumors. Dissociated cancer cells from autochthonous tumors also displayed a pronounced differential response to the two TAM populations, with TAMs harvested from control tumors being more effective at supporting tumor cell growth (Figures S4F and S4G) and lung metastasis (Figure S4H) than TAMs isolated from Treg cell ablated mice. Finally, we evaluated whether co-injected TAMs could still modulate tumor cell growth when transplanted into a lymphoreplete host, in which the recipient's niche is occupied. As expected, in these challenging conditions, the resulting tumor modulation was considerably less pronounced in

both EO771 (Figure S4I) and PyMT (Figure S4J) cells, although it was still significant in the EO771 model (Figure S4I).

The group of experiments performed on severely immunocompromised hosts suggests that at least part of the effector function of TAMs over tumor cells does not require crosstalk with the adaptive immune system beyond that taking place immediately after Treg cell ablation. To test whether TAMs can directly affect tumor cell growth, we co-cultured sorted TAMs and luciferase-transduced tumor cells *in vitro* at equal ratios, and quantified their relative amounts by bioluminescence imaging 72 h after initial plating (Figure S4K). We found that the co-culture of TAMs from control tumors resulted in a significantly higher number of tumor cells compared to TAMs sorted from tumors without Treg cells (Figures S4L and S4M).

In summary, our experiments indicate that Treg cell ablation leads to a functional reprogramming of TAMs, which in turn are sufficient to drive anti-tumor responses at least partially through the direct induction of tumor cell death.

TAM Functional Reprogramming Is Mediated by CD4$^+$ T Cell-Derived Increase in IFN-γ

An unbiased cytokine array in our previous study identified IFN-γ and its target genes CXCL9 and CXCL10 as the most upregulated cytokine and chemokines in Treg cell-ablated tumor lysates (Bos et al., 2013). Furthermore, antibody-mediated neutralization of IFN-γ abolished the anti-tumor effect caused by Treg cell ablation (Bos et al., 2013). In addition, by isolating different leukocyte populations from tumors, we determined that IFN-γ target genes were significantly upregulated in the tumor-associated myeloid cell compartment upon Treg cell ablation (Bos et al., 2013). These observations, together with the essential role of IFN-γ as a macrophage polarizing factor (Alspach et al., 2018) led us to formally test the critical role of IFN-γ in the functional TAM reprogramming observed upon Treg cell ablation. We took a loss-of-function approach by crossing *Ifnγr2*^{FLOX} mice (Lee et al., 2015) with *LysM*^{CRE} and *Foxp3*^{DTR} mice to produce animals in which myeloid cells are insensitive to IFN-γ signaling due to the deletion of the IFNGR2 receptor, and Treg cells can be conditionally ablated by DT treatment. Importantly, PyMT and EO771 orthotopic primary tumor growth and lung metastasis were unaffected in the mice lacking IFN-γ signaling in the myeloid compartment but with functional Treg cells (Figures 5A–5D). However, Treg cell ablation-dependent reduction in primary tumor and lung metastasis growth was severely compromised in *Ifngr2*^{FLOX} *LysM*^{CRE} *Foxp3*^{DTR} mice in both PyMT and EO771 tumor models (Figures 5A–5D). These experiments suggest that myeloid-specific IFN-γ signaling is critical for the anti-tumor phenotype elicited by Treg cell ablation.

We then decided to test whether IFN-γ signaling is sufficient to confer anti-tumor function to bone marrow monocytes from tumor-bearing mice. To this end, we harvested Ly6C$^+$ inflammatory monocytes from the bone marrow of *Ccr2*^{GFP} *Foxp3*^{DTR} double transgenic mice bearing orthotopic PyMT or EO771 tumors and treated them *ex vivo* with 100 U/mL recombinant IFN-γ for 30 min. Immediately after treatment, we washed and transferred the “primed” or “mock-treated” monocytes intravenously into control *Foxp3*^{DTR} tumor-bearings hosts and followed tumor growth over time (Figures 5E–5H). To our surprise, whereas

untreated inflammatory monocyte transfer had no effect on tumor growth, the short ex vivo treatment of the monocytes with IFN-γ followed by a single infusion into the tumorbearing mice resulted in a significant reduction in primary tumor growth (Figures 5E–5H). Of note, this effect was not strong enough to achieve lung metastasis reduction (Figure S5), consistent with our previous CCR2 ablation study, once again highlighting the fact that the biology behind the Treg cell-suppressive effect at the metastatic site may be different, and it needs to be investigated further.

Next, we attempted to evaluate whether the source of IFN-γ was $CD4^+$ T lymphocytes. We have previously shown that $CD4^+$ T cell depletion blunts the anti-tumor effect driven by Treg cell ablation (Bos et al., 2013), but not depletion of CD8 T cells or NK cells, hinting at a critical role of $CD4^+$ T cell-specific IFN-γ production. Therefore, we generated *Foxp3*^{DTR} *Ifng*^{KO} mice and performed adoptive transfer of $CD4^+$ T cells from *Foxp3*^{DTR} *Ifng*^{KO} and *Foxp3*^{DTR} *Ifng*^{WT} mice into $RAG^{-/-}$ mice. We then orthotopically injected PyMT cells and performed Treg cell ablation (Figure 6A). In this setting, Treg cell targeting drives an anti-tumor phenotype only in the mice receiving $CD4^+$ T cells from *Foxp3*^{DTR} *Ifng*^{WT} mice (Figures 6B–6D), suggesting that the $CD4^+$ T IFN-γ production is the main contributor to the anti-tumor phenotype.

Our data support the hypothesis that Treg cells promote breast cancer progression and lung metastasis through opposing the role of $CD4^+$ T cell-derived IFN-γ on the inflammatory monocyte and TAM compartments.

Gene Expression Changes Driven by Treg Cell Ablation in TAMs Are Predictive of Better Prognosis in Human Breast Cancer

To achieve clinical relevance for our findings in mouse models, we turned to bioinformatics analysis of mouse and human samples. We sorted TAMs from mock- or DT-treated primary EO771derived tumors as before, and performed genome-wide RNA sequencing analysis to identify gene expression profiles in the TAM compartment caused by Treg cell ablation. A set of 92 genes was differentially expressed between these groups, with a false discovery rate (FDR) ≤0.05 and an absolute $\log_2$ fold change ≥ 1.4 (Figure 7A; Table S1). In line with our previously published cytokine/chemokine screen performed on tumor lysates (Bos et al., 2013), among the upregulated genes, we could identify the IFN-γ-induced chemokines CXCL9, CXCL10, and CXCL11. Notably, IFN-γ itself and other IFN-γ-inducible genes such as PD-L1, IDO1, and Nos2 (slightly below the fold change cutoff value we set) were among the upregulated list, consistent with our experimental findings. We reasoned that a similar gene expression pattern in the breast cancer patient population may be associated with better survival, and interrogated a set of 1,095 breast cancer patient samples from The Cancer Genome Atlas (TCGA) (The Cancer Genome Atlas, 2012). Of the 92 genes identified in the mouse samples, 71 had human orthologs that we used to cluster the human samples (Figure S6A). Upon initial analysis, we found that this gene set identified a distinct cluster of patients with a similar gene expression pattern to the upregulated genes in the mouse signature (Figure S6A). However, the genes that were downregulated in the mouse signature did not have consistent expression profiles in the human population (Figure S6B). Therefore, we chose to re-cluster the human samples with the 55 human orthologs

corresponding to the upregulated genes in the list. This new analysis revealed a group of patients with similar gene expression pattern to the one from Treg cell-ablated TAMs that we called “DT-like,” another cluster of patients with similar expression profiles to the control TAMs that we called “control-like,” and a large group of patients with intermediate profiles (“intermediate”) (Figure 7B). The immune content of tumors in the TCGA dataset has recently been assessed (Thorsson et al., 2018) and the estimate of different immune cell fractions in each tumor was made available. Given that our gene set is derived from TAMs and reflects their state of classical activation, we wondered if the resulting clustering reflected the M1/M2 macrophage composition of the tumors analyzed. Interestingly, we observed that the “DT-like” cluster of samples was enriched in M1 macrophages ($p < 1.14e–67$), and the “control-like” cluster was enriched in M2 macrophages ($p < 3.3e–60$) (Figure 7B). To investigate whether patients with a DT-like profile would have a better outcome, we performed Kaplan-Meier survival analysis comparing them with the control-like cluster. Interestingly, the DT-like patient cluster had significantly better survival than the control-like cluster (Figure 7C). ER status is a distinct driver of breast cancer biology and a strong independent predictor of outcome (Osborne et al., 1980). Cell intrinsic features of tumors dictate the composition of their immune infiltrate (Wellenstein and de Visser, 2018; Wang et al., 2017; Spranger et al., 2015). We wondered whether this TAM-derived signature was able to predict outcome independently of ER status, and used it to interrogate the 761 patients annotated as ER^+ and the 231 patients annotated as ER independently. This mouse-derived gene signature was still able to predict outcomes in the group of ER^+ patients (Figure 7D), while there was a non-significant trend in the ER group (Figure 7E). We noticed that, while significant, the survival analysis on the ER^+ samples seemed less efficient than the analysis of the complete group, suggesting to us that the mouse-derived signature is strongly but not completely associated with ER^+ status.

This analysis presents clinical evidence that the changes elicited by Treg cell ablation on TAMs are consistent with improved survival in human breast cancer, supporting the biological relevance of our experimental findings.

DISCUSSION

Recruitment of Treg cells into the tumor microenvironment is a potent immunosuppressive mechanism in a variety of cancer types. Targeting intratumoral Treg cells typically leads to an enhanced cytotoxic cell response driven by CD8 T cells (Klages et al., 2010; Jang et al., 2017) or NK cells (Teng et al., 2010). In murine breast cancer models, however, we have previously shown that these cell types are dispensable for the anti-tumor activity, although a strong IFN-γ response ensues (Bos et al., 2013).

TAMs are critical regulators of tumor growth, progression, and response to therapy. Mammary gland TAMs originate from bone-marrow-derived monocytes. A correlation between inflammatory monocytes and Treg cells has been noticed before in the metallothionein 1-driven Ret oncogene (Mt1/ret) melanoma mouse model, in which targeting Treg cells by anti-CD25 or anti-interleukin-10 (IL-10) treatment diminishes tumor cell dissemination, with a concomitant increase in inflammatory monocytes, suggesting that Treg cells may act by somehow opposing their recruitment and/or differentiation (Pommier

et al., 2013). In our present work, using loss-of-function genetic approaches and gain-of-function adoptive transfers, we found that monocyte recruitment is essential to achieve a significant response to Treg cell ablation *in vivo*, convincingly demonstrating that they are the main effector cell type driving the anti-tumor phenotype. Interestingly, while we did not observe any significant difference in the amount of inflammatory monocytes or TAMs recruited to tumors upon Treg cell ablation, we went on to show that they produce functionally distinct macrophages with a diminished ability to support tumor cell growth *in vitro* and *in vivo*. Whether TAMs acquire the ability to kill tumor cells or lose the property of stimulating tumor cell growth, or a combination of both, is a question that remains to be addressed. Chief among the genes that become upregulated in the TAM compartment is Nos2, hinting at the production of reactive oxygen species as possible effector mechanisms. In addition, there are high levels of CXCL9 and CXCL10, and a number of extracellular matrix remodeling factors, suggesting that microenvironmental remodeling also plays a role.

We have previously detected a significant increase in IFN-γ and IFN-γ-driven chemokines in primary tumor lysates upon Treg cell ablation (Bos et al., 2013). Moreover, we had observed that while tumor-infiltrating T cells displayed a significant increase in IFN-γ production, myeloid cells from those tumors exhibited an enhanced response to the cytokine upon Treg cell ablation (Bos et al., 2013). Work in a muscle injury model where Treg cells have been shown to facilitate fiber regeneration demonstrated an enhanced IFN-γ response on major histocompatibility complex class II-positive ($MHCII^+$) macrophages upon Treg cell targeting (Panduro et al., 2018). A recent article by Liu et al. (2019) using B16 and MC38 cell lines showed that Treg cells induce an M2-like phenotype on TAMs through suppressing IFN-γ production on CD8 T cells. However, interfering with this reprogramming did not result in any detectable tumor phenotype (Panduro et al., 2018). In our present work, we demonstrate that the anti-tumoral function acquired by monocytes/TAMs in the DT-treated tumors requires IFN-γ sensing, as conditional deletion of the IFNGR2 in myeloid cells almost completely negates the phenotype. Moreover, a brief *ex vivo* exposure of inflammatory monocytes to recombinant IFN-γ followed by adoptive transfer into tumor-bearing mice recapitulates the anti-tumor effect to a significant degree. Thus, the present study firmly demonstrates that Treg cells support breast cancer growth by preventing a high level of IFN-γ production and its consequent IFN-γ-dependent functional reprogramming of monocytes/macrophages. Importantly, we observed that a subset of human breast tumor samples displays similar gene expression profiles to that of TAMs upon Treg cell ablation. Furthermore, they have better overall survival when compared with samples that resemble TAM gene expression profiles from control tumors. Moreover, this subset of tumors shows enrichment in M1-like TAMs. This observation supports the functional relevance of the murine mechanism described. Furthermore, our experiments strongly suggest that the critical source of IFN-γ in breast cancer models is the $CD4^+$ T cell compartment, but more stringent genetic studies must be performed to fully confirm this observation.

Interestingly, while Treg cell ablation has a profound effect on lung metastasis growth, the downstream role of bone-marrow-derived monocytes was less evident. In the present work, all of the mechanistic studies evaluated the effects on lung metastasis developing spontaneously from the orthotopic breast tumor. This process is complex, including

dissemination from the primary tumor, seeding of the lungs, and outgrowth (Bos et al., 2010), which results in a large biological variation that may be responsible for the heterogeneous effects. However, it is also possible that the diverse tissue microenvironment in which metastasis arises is subjected to different biological processes. Ongoing experimental metastasis studies are aimed at elucidating these important differences.

These observations strongly support a model in which Treg cells prevent IFN-γ-driven classical activation of monocyte/macrophages recruited to the tumors by suppressing $CD4^+$ T cell cytokine production, compromising their anti-tumor activities and leading to enhanced primary and metastatic breast tumor growth. Furthermore, our work raises the possibility that monocytes from cancer patients can be reprogrammed ex vivo through brief exposure to IFN-γ and re-infused into patient circulation, contributing to the generation of anti-tumor responses. While intratumoral injection of IFN-γ could also result in similar anti-tumor effects, prolonged treatment would likely result in undesired secondary effects (Parker et al., 2016) and lead to the induction of resistance mechanisms that negate the benefit (Benci et al., 2016). A recent study in support of this therapeutic possibility is the engineering of IFN-γ particles (backpacks) that attach to macrophage surfaces and can reprogram them, conferring some anti-tumor effects in the 4T1 breast cancer model (Shields et al., 2020). Finally, our results hold true in tumor models that are either insensitive (PyMT) or partially sensitive (EO771) to immune checkpoint blockade, suggesting that targeting the myeloid compartment is a valuable broad approach for all breast cancers, offering an alternative for the majority of patients in whom ICB is not an option. Further studies will attempt to better understand the relevant changes on the monocyte compartment induced by IFN-γ and optimize adoptive transfer approaches with therapeutic purpose.

STAR★METHODS

Detailed methods are provided in the online version of this paper and include the following:

RESOURCE AVAILABILITY

Lead Contact—Further information and request for reagents should be directed to and will be fulfilled by the Lead Contact, Paula D. Bos, PhD (paula.bos@vcuhealth.org).

Materials Availability—This study did not generate new unique reagents.

Data and Code Availability—The RNASequence data generated during this study has been deposited in GEO: GSE159806.

All code used in this study is available at: https://github.com/AmyOlex/Clark_Bos_2020_TregsOpposeIFNgReprogOfMyeloidCells

EXPERIMENTAL MODEL AND SUBJECT DETAILS

Mice—*Foxp3*$^{DTR\text{-}GFP}$ mice were a gift provided by A. Rudensky (Memorial Sloan Kettering Cancer Center, New York, NY). *Ccr2*$^{DTR\text{-}CFP}$ and *Ccr2*^{GFP} mice were kindly provided by E. Pamer (Memorial Sloan Kettering Cancer Center, New York, NY). *Ifnγr2*^{flox} mice (Lee et al., 2015) were obtained from L. Lu (University of California, San Diego).

C57BL/6 *MMTV-PyMT* mice were a gift from M.O. Li (Memorial Sloan Kettering Cancer Center, New York, NY). *LysMcre* (Stock #004781), NOD-*scidIL2Rgamma*^{null} (NSG, Stock #005557) and *Ifng*^{KO} mice (Stock #002287) were purchased from the Jackson Laboratories. For all experiments, age-matched virgin females, 6–9 weeks of age were used. All animal experiments were performed in accordance with the Virginia Commonwealth University Institutional Animal Care and Use Committee.

Cell Lines—PyMT cell lines were obtained previously from dissociated MMTV-PyMT tumor-bearing mice (Bos et al., 2013). EO771 cell line was obtained from C3H Biosystems, and transduced with a lentiviral vector containing thymidine kinase 1, green fluorescent protein and firefly luciferase (TGL), as previously described (Bos et al., 2013). BRPKP110 cell line was obtained from the Wistar Institute (Rutkowski et al., 2015). All cell lines were expanded in Dulbecco's modified Eagle's, high glucose medium supplemented with 10% FBS and pen.

METHOD DETAILS

Animal Experiments—For orthotopic implantation experiments, 150,000 tumor cells were re-suspended in PBS and mixed at a 1:1 ratio with growth factor reduced Matrigel (BD). Cell suspension was injected bilaterally (unless specified) into the fourth mammary gland of isoflurane-anesthetized mice. Primary tumor growth was monitored three times a week by taking measurements of tumor length (L) and width (W). Tumor volume was calculated using the formula $\pi LW^2/6$. Primary tumors were harvested at the humane end-point and weighed for total tumor burden. Lung metastatic burden was determined by *ex vivo* bioluminescence imaging using an IVIS-200 imaging system (Xenogen Corp.). To this end, mice were anesthetized and injected retro-orbitally with 1.5mg of D-Luciferin (15mg/ml), sacrificed 2 min after injection, and lung imaging completed within the next 5 min. Alternatively, when cells were not transduced with luciferase, lung metastatic burden was calculated by counting lung metastatic nodules under a dissection stereomicroscope (for MMTV-PyMT mouse experiments).

Adoptive Transfer Experiments—*Ccr2*^{GFP} *Foxp3*$^{DTR\text{-}GFP}$ donor mice and *Ccr2*$^{DTR\text{-}CFP}$ *Foxp3*$^{DTR\text{-}GFP}$ recipient mice were injected with either PyMT or EO771 cell lines as mentioned above, at the same time. Primary tumors were allowed to grow until they became palpable but did not exceed 90mm^3. The femurs were then harvested from the donor mice, and the bone marrow was flushed through a 100 μm filter. Red blood cells were lysed using ACK red blood cell lysis buffer, cells were counted using a hemocytometer and re-suspended in MACS buffer. Cell suspensions were stained with anti-CD11B (M1/70, 1:1000, eBioscience), anti-Ly6C (HK1.4, 1:1000, eBioscience), and anti-Ly6G (1A8, 1:1000, eBioscience). CCR2$^+$ CD11B$^+$ Ly6C$^+$ Ly6G$^-$ bone-marrow-derived cells were sorted using a FACSAria II high-speed cell sorter (BD) placed in a BSL2 biosafety cabinet, collected into complete medium, and washed and resuspended in PBS for injection. 250,000 sorted inflammatory monocytes were injected i.v. into the *Ccr2*$^{DTR\text{-}CFP}$ *Foxp3*$^{DTR\text{-}GFP}$ recipient mice, which received 50 mg/kg diphtheria toxin (DT) 6 h prior to adoptive transfer, and a second dose 24 hr. after. For IFN-γ pre-treatment experiments, sorted cells were collected and maintained in medium containing 100U/ml of IFN-γ for 30 min, and then

washed and injected. Tumor progression and metastatic burden were measured as mentioned above.

For $CD4^+$ T cell adoptive transfers, $CD4^+$ T cells were isolated from pooled spleen and lymph nodes of *Foxp3*^{DTR} *Ifng*^{KO} and *Foxp3*^{DTR} *Ifng*^{WT} mice using CD4 positive isolation (Dynal Beads, Invitrogen) following manufacturer's instructions. 1.5 million $CD4^+$ T cells were injected intravenously into each recipient $RAG^{-/-}$ mouse, and PyMT cells were injected orthotopically 24 hr. after transfer. Tumor progression and burden was measured as described.

Tumor Associated Macrophage Co-Injection Experiments—*Foxp3*$^{DTR\text{-}GFP}$ donor mice were injected as mentioned above with either PyMT or EO771 cells, and their tumors were allowed to grow until approximately $90mm^3$. Half of the donors received two doses of 50 mg/kg of diphtheria toxin (DT) in two consecutive days, and primary tumors from both groups were harvested four days after initial DT treatment. For MMTV-PyMT, mice were treated at a similar tumor size, when mice were 14–18 weeks old. Tumor-associated macrophages were isolated as previously described (Clark and Bos, 2019). Briefly, the primary tumors were enzymatically disassociated with 0.5 mg/mL of Liberase TL (Roche) and digested following manufacturer's instructions. The resulting digestion mixture was filtered through a 100 mm filter to obtain a single cell suspension. $CD11B^+$ cells were positively enriched by magnetic bead isolation (Dynal Beads, Invitrogen) prior to cell sorting following manufacturer's instructions. The enriched myeloid population was then stained for cell sorting using anti-CD11B (M1/70, 1:1000, eBioscience), anti-Ly6C (HK1.4, 1:1000, eBioscience), anti-Ly6G (1A8, 1:1000, eBioscience), and anti-F4/80 (BM8, 1:1000, eBioscience). Live cells ($DAPI^-$) were gated on $CD11B^+$ $Ly6G^-$ $F4/80^+$ and collected for downstream applications. For *in vivo* co-injection with tumor cells, TAMs were mixed at a 1:1 ratio (50,000 TAMs with 50,000 tumor cells or whole dissociated cells from spontaneous MMTV-PyMT tumors) and injected unilaterally into the fourth mammary gland of anesthetized NSG mice. Tumor progression and metastatic burden were measured as mentioned above. For co-culture experiments, 50,000 TAMs were plated on 96-well plates over a monolayer of 50,000 tumor cells, and placed in an incubator for 72 h. At the end point, culture wells were imaged by adding of 150 mg/mL D-luciferin, incubated 2 min and imaged by bioluminescence imaging using an IVIS200 Imaging System (Xenogen Corp.)

FACS Analysis—Whole tumor infiltrating leukocytes population dynamics were determined by enzymatically disassociating primary tumors from *Ccr2*^{GFP} *Foxp3*$^{DTR\text{-}GFP}$ mice as mentioned above. TAM activation markers were determined by disassociating primary tumors of *Foxp3*$^{DTR\text{-}GFP}$ tumor bearing mice 4 days after intervention as described above. Cell suspensions were stained with anti-CD45 (30F11, 1:1000, BD Bioscience), Ghost Violet Viability (1:2000, Tonbo Bioscience), (anti-CD11B (M1/70, 1:1000, eBioscience), anti-CD4 (RM4–5, 1:1000, Tonbo Bioscience), anti-CD8a (53–6.7, 1:800, eBioscience), anti-CD19 (1D3, 1:1000, Tonbo Bioscience), antiCD11c (HL3, 1:1000, BD Bioscience), anti-NK1.1 (PK136, 1:1000, Tonbo Bioscience), anti-F4/80 (BM8, 1:1000, eBioscience), anti-Ly6C (HK1.4, 1:1000, eBioscience), anti-Ly6G (1A8, 1:1000, eBioscience), anti-MHCII (M5/114.15.2, 1:800, Tonbo Bioscience), anti-CD86 (GL1, 1:500,

BD Bioscience), anti-CD80 (16–10A1, 1:500, BD Bioscience), and anti-FoxP3 (FJK-16S, 1:500, Invitrogen). Stained cells were analyzed with a LSRII Fortessa flow cytometer (BD) from the VCU Flow Cytometry Core Facility. Data were analyzed using FlowJo software (Tree Star).

Histology—For histological analysis, tissues were fixed in 4% paraformaldehyde solution for 30 min at room temperature, after which they were processed for immunohistochemistry (IHC). Tumor cell apoptosis was determined by IHC staining for cleave-caspase 3 using standard IHC protocols. The primary cleaved-caspase 3 antibody (Cat#9661, Cell Signaling Technologies) was used at a 1:625 dilution and the secondary biotinylated antibody (Cat#BA-1000, Vector Laboratories) was used at a 1:1000 dilution. Tumor associated macrophage numbers were determined by Iba-1 or F4/80 immunofluorescence, using standard protocols on frozen sections fixed as described above. The primary Iba-1 antibody (Cat# 019–19741, Wako) was used at a 1:500 dilution, the F4/80 antibody (Cat# ab6640) was used at 1:100 dilution and the secondary (Cat#A31634 Life Technologies or Cat#FI-4001, Vector Labs) was used at a 1:1000 dilution.

RNA Sequencing—TAMs were sorted as described, and collected into TrizolLS (Thermo Fisher) for subsequent RNA isolation. RNA isolation was performed following manufacturer's protocols. Initial quality control was performed using an Agilent Bioanalizer System through the Pathology Tissue and Data Acquisition and Analysis Core (TDAAC). All samples were sent to the Brigham Young University DNA sequencing core for further library construction and sequencing. KAPA Stranded mRNA-Seq Kit was used for library preparation. Samples were sequenced on the Illumina Hi-Seq 2500 according to Illumina's sequencing-by-synthesis protocol. 125bp pairedend reads were generated, yielding on average 87M reads per sample.

RNA Sequencing Preprocessing—FastQC v.0.11.5 (Andrews, 2010) was used for quality control at all stages of RNA-seq preprocessing. The Mouse GRCm38/mm10 reference genome was obtained from UCSC Genome Browser Gateway (http://hgdownload.soe.ucsc.edu/goldenPath/mm10/bigZips/chromFa.tar.gz), and the corresponding gene annotation file was obtained from Ensemble (ftp://ftp.ensembl.org/pub/release-83/gtf/mus_musculus/Mus_musculus.GRCm38.83.gtf.gz) on 02/20/2016. Only autosomes, mitochondrial, and sex chromosomes were used.

Reads were trimmed with Trimmomatic v.0.33 (Bolger et al., 2014) and aligned to the indexed reference genome using Subread v1.6.2 (Liao et al., 2013). Read counting on a transcript reference file was performed using Subread's "featureCounts" algorithm. The counts were imported into R v.3.4.0 (R Development Core Team, 2017) and the log2 transformed Transcripts per Million (TPM) values were calculated using an in-house script and used for all analyses. Heatmaps of Pearson's correlation coefficients between all sample-specific gene expression profiles were plotted with the NMF R package v.0.22.0 (Gaujoux and Seoighe, 2010) aheatmap() function using Hierarchical clustering with Euclidean distance and Ward linkage.

Differential Gene Expression Analysis—A differential expression analysis was performed on TAMs sorted from control EO771 primary tumors and TAMs sorted from DTtreated EO771 primary tumors using raw reads counts. Genes with a read count of zero for all samples were removed prior to identifying differentially expressed genes using the DESeq2 R package v.1.16.1 (Love et al., 2014). Genes are considered significantly differentially expressed if the Benjamini-Hochberg adjusted p value is ≤ 0.05 and the absolute value of the Log2 Fold Change is > = 1.4. The list of differentially expressed genes was filtered to those that were upregulated (Log2 FC > = 1.4) in DT-treated samples compared to control. All genes meeting this cutoff comprise the EO771 gene signature.

TCGA Gene Expression Analysis—Legacy RSEM scaled estimates for The Cancer Genome Atlas Breast Cancer cohort (TCGA-BRCA)(The Cancer Genome Atlas Network, 2012) were downloaded using the GDCQuery function of the TCGABiolinks v2.5.9 (Colaprico et al., 2016) Bioconductor (Huber et al., 2015) R package with the following settings: project = c("TCGA-BRCA"), file.type = "rsem.genes.results," platform = "Illumina HiSeq," legacy = TRUE, sample.type = "Primary solid Tumor," data.category = "Gene expression," data.type = "Gene expression quantification," experimental.strategy = "RNA-Seq." Scaled estimates were converted into Log2 TPM values as described in Li and Dewey (2011), and then upper quartile normalized. The 92 mouse gene signature Ensemble IDs were input into UCSF's OrthoRetriever (https://lighthouse.ucsf.edu/orthoretriever/) to identify the orthologous human gene symbols and Entrez IDs, which resulted in 71 human genes for analysis in the TCGA cohort (55 corresponded to highly expressed mouse genes, and 16 to lowly expressed mouse genes). The human gene symbol and Entrez ID were then used to extract the corresponding gene expression profiles from the TCGA-BRCA dataset.

Row-median centered and normalized Log2 TPM expression profiles for the TCGA data were clustered using the aheatmap() function in R's NMF package using Euclidean distance and Ward linkage, and divided into 3 clusters. Patients in the cluster with the majority of high expressed genes were classified as "DT-like," patients in the cluster with the majority of low expressed genes were classified as "Control-like," and the third cluster containing a mixture of mild high and low expression was classified as "Intermediate." Macrophage 1 and 2 signatures were taken from Thorsson et al. (2018) for the TCGA BRCA cohort with low/medium/high thresholds being calculated using the 25th and 75th percentile across all patients for each signature (excluding those with an NA value). Thresholds for M1 are high > = 0.088 and low < 0.032, and for M2 are high > = 0.354 and low < 0.189 with mid being assigned to all other patients with values other than NA. TCGA patients were grouped into ER+/ cohorts using the "er_status_by_ihc" column from the GDC TCGA Legacy Archive biotab clinical files (accessed on 7/9/2018).

TCGA Survival Analysis—Survival data for 1078 patients in the TCGA-BRCA cohort was obtained from the National Cancer Institute's Genomic Data Commons (GDC) Data Portal (Grossman et al., 2016) exploration page on 7/9/2018. All patients with data past 10 years (3650 days) were censored as alive at this time point to obtain 10-year overall survival. Kaplan-Meier survival curves and Log-Rank p values were calculated using R's survival v2.42–6 (Therneau and Grambsch, 2010) and survminer v0.4.2 (Kassambara et al., 2018)

packages. Hazard ratios of DT-like versus Control were calculated using the Cox proportional-hazards model function that is part of the survival package.

QUANTIFICATION AND STATISTICAL ANALYSIS

All statistical analysis was performed using GraphPad Prism V7 software. Unpaired and paired Student's t tests, one-way analysis of variance (ANOVA) with post-test Tukey HSD's multiple comparisons, and two-way ANOVA with multiple comparisons were used as described in the legend figures. Non-parametric analyses were performed when appropriate and denoted in the figure legend of the corresponding figures. Results are presented as means ± SEM p values of less than 0.05 were considered statistically significant.

Supplementary Material

Refer to Web version on PubMed Central for supplementary material.

ACKNOWLEDGMENTS

We are grateful to S. Rudensky (MSKCC) for advice and the generous gift of various mouse strains; M. Rutkowski (UVA) and J. Conejo-Garcia (Moffit) for the BRPKP100 cell line; D. Conrad (VCU), A. Atfi (VCU), J. González-Maeso (VCU), and H. Bear (VCU) for critical reading of the manuscript; and C. Harrell (VCU) for advice on bioinformatics analysis. This work was supported by Virginia Commonwealth Department of Pathology startup funds (P.D.B.), American Cancer Society Institutional Research Grant no. 14–192-40 (P.D.B.), and partially by METAvivor Research and Support Inc. (P.D.B.) and Susan G. Komen Career Catalyst Grant CCR18548205 (P.D.B.) awards. A.L.O. was supported by CTSA award UL1TR002649 from the National Center for Advancing Translational Sciences. Services obtained through the VCU Massey Cancer Center Flow Cytometry and Mouse Models Shared Resource were supported, in part, with funding from NIH-NCI Cancer Center Support Grant P30 CA016059.

REFERENCES

Alexandrov LB, Nik-Zainal S, Wedge DC, Aparicio SA, Behjati S, Biankin AV, Bignell GR, Bolli N, Borg A, Børresen-Dale AL, et al.; Australian Pancreatic Cancer Genome Initiative; ICGC Breast Cancer Consortium; ICGC MMML-Seq Consortium; ICGC PedBrain (2013). Signatures of mutational processes in human cancer. Nature 500, 415–421. [PubMed: 23945592]

Alspach E, Lussier DM, and Schreiber RD (2018). Interferon gamma and Its Important Roles in Promoting and Inhibiting Spontaneous and Therapeutic Cancer Immunity. Cold Spring Harb. Perspect. Biol. 11, a028480.

Andrews S. (2010). FastQC: a quality control tool for high throughput sequence data.. http://www.bioinformatics.babraham.ac.uk/projects/fastqc.

Azizi E, Carr AJ, Plitas G, Cornish AE, Konopacki C, Prabhakaran S, Nainys J, Wu K, Kiseliovas V, Setty M, et al. (2018). Single-Cell Map of Diverse Immune Phenotypes in the Breast Tumor Microenvironment. Cell 174, 1293–1308.e36. [PubMed: 29961579]

Benci JL, Xu B, Qiu Y, Wu TJ, Dada H, Twyman-Saint Victor C, Cucolo L, Lee DSM, Pauken KE, Huang AC, et al. (2016). Tumor Interferon Signaling Regulates a Multigenic Resistance Program to Immune Checkpoint Blockade. Cell 167, 1540–1554.e12. [PubMed: 27912061]

Bolger AM, Lohse M, and Usadel B. (2014). Trimmomatic: a flexible trimmer for Illumina sequence data. Bioinformatics 30, 2114–2120. [PubMed: 24695404]

Bos PD, Nguyen DX, and Massagué J. (2010). Modeling metastasis in the mouse. Curr. Opin. Pharmacol. 10, 571–577. [PubMed: 20598638]

Bos PD, Plitas G, Rudra D, Lee SY, and Rudensky AY (2013). Transient regulatory T cell ablation deters oncogene-driven breast cancer and enhances radiotherapy. J. Exp. Med. 210, 2435–2466. [PubMed: 24127486]

Clark NM, and Bos PD (2019). Tumor-Associated Macrophage isolation and in vivo analysis of their tumor promoting activity. Methods Mol. Biol. 1884, 151–160. [PubMed: 30465201]

Colaprico A, Silva TC, Olsen C, Garofano L, Cava C, Garolini D, Sabedot TS, Malta TM, Pagnotta SM, Castiglioni I, et al. (2016). TCGAbiolinks: an R/Bioconductor package for integrative analysis of TCGA data. Nucleic Acids Res. 44, e71. [PubMed: 26704973]

Denkert C. (2014). The immunogenicity of breast cancer–molecular subtypes matter. Ann. Oncol. 25, 1453–1455. [PubMed: 24950977]

Dunn GP, Ikeda H, Bruce AT, Koebel C, Uppaluri R, Bui J, Chan R, Diamond M, White JM, Sheehan KC, and Schreiber RD (2005). Interferon-gamma and cancer immunoediting. Immunol. Res. 32, 231–245. [PubMed: 16106075]

Dwyer RM, Potter-Beirne SM, Harrington KA, Lowery AJ, Hennessy E, Murphy JM, Barry FP, O'Brien T, and Kerin MJ (2007). Monocyte chemotactic protein-1 secreted by primary breast tumors stimulates migration of mesenchymal stem cells. Clin. Cancer Res. 13, 5020–5027. [PubMed: 17785552]

Ewens A, Mihich E, and Ehrke MJ (2005). Distant metastasis from subcutaneously grown E0771 medullary breast adenocarcinoma. Anticancer Res. 25 (6B), 3905–3915. [PubMed: 16312045]

Franklin RA, Liao W, Sarkar A, Kim MV, Bivona MR, Liu K, Pamer EG, and Li MO (2014). The cellular and molecular origin of tumor-associated macrophages. Science 344, 921–925. [PubMed: 24812208]

Gaujoux R, and Seoighe C. (2010). A flexible R package for nonnegative matrix factorization. BMC Bioinformatics 11, 367. [PubMed: 20598126]

Grossman RL, Heath AP, Ferretti V, Varmus HE, Lowy DR, Kibbe WA, and Staudt LM (2016). Toward a Shared Vision for Cancer Genomic Data. N. Engl. J. Med. 375, 1109–1112. [PubMed: 27653561]

Herschkowitz JI, Simin K, Weigman VJ, Mikaelian I, Usary J, Hu Z, Rasmussen KE, Jones LP, Assefnia S, Chandrasekharan S, et al. (2007). Identification of conserved gene expression features between murine mammary carcinoma models and human breast tumors. Genome Biol. 8, R76. [PubMed: 17493263]

Hohl TM, Rivera A, Lipuma L, Gallegos A, Shi C, Mack M, and Pamer EG (2009). Inflammatory monocytes facilitate adaptive CD4 T cell responses during respiratory fungal infection. Cell Host Microbe 6, 470–481. [PubMed: 19917501]

Huber W, Carey VJ, Gentleman R, Anders S, Carlson M, Carvalho BS, Bravo HC, Davis S, Gatto L, Girke T, et al. (2015). Orchestrating high throughput genomic analysis with Bioconductor. Nat. Methods 12, 115–121. [PubMed: 25633503]

Jang JE, Hajdu CH, Liot C, Miller G, Dustin ML, and Bar-Sagi D. (2017). Crosstalk between Regulatory T Cells and Tumor-Associated Dendritic Cells Negates Anti-tumor Immunity in Pancreatic Cancer. Cell Rep. 20, 558–571. [PubMed: 28723561]

Josefowicz SZ, Lu LF, and Rudensky AY (2012). Regulatory T cells: mechanisms of differentiation and function. Annu. Rev. Immunol. 30, 531–564. [PubMed: 22224781]

Joshi NS, Akama-Garren EH, Lu Y, Lee DY, Chang GP, Li A, DuPage M, Tammela T, Kerper NR, Farago AF, et al. (2015). Regulatory T Cells in Tumor-Associated Tertiary Lymphoid Structures Suppress Anti-tumor T Cell Responses. Immunity 43, 579–590. [PubMed: 26341400]

Kassambara A, Kosinski M, Biecek P, and Fabian S. (2018). Survminer: Drawing Survival Curves using 'ggplot2'.https://rdrr.io/cran/survminer/.

Klages K, Mayer CT, Lahl K, Loddenkemper C, Teng MW, Ngiow SF, Smyth MJ, Hamann A, Huehn J, and Sparwasser T. (2010). Selective depletion of Foxp3+ regulatory T cells improves effective therapeutic vaccination against established melanoma. Cancer Res. 70, 7788–7799. [PubMed: 20924102]

Lanc a, T., Costa MF, Gonç alves-Sousa N, Rei M, Grosso AR, Penido C, and Silva-Santos B. (2013). Protective role of the inflammatory CCR2/ CCL2 chemokine pathway through recruitment of type 1 cytotoxic gd T lymphocytes to tumor beds. J. Immunol. 190, 6673–6680. [PubMed: 23686489]

Lee HM, Fleige A, Forman R, Cho S, Khan AA, Lin LL, Nguyen DT, O'Hara-Hall A, Yin Z, Hunter CA, et al. (2015). IFNg signaling endows DCs with the capacity to control type I inflammation

during parasitic infection through promoting T-bet+ regulatory T cells. PLOS Pathog. 11, e1004635.

Li B, and Dewey CN (2011). RSEM: accurate transcript quantification from RNA-Seq data with or without a reference genome. BMC Bioinformatics 12, 323. [PubMed: 21816040]

Li X, Kostareli E, Suffner J, Garbi N, and Hämmerling GJ (2010). Efficient Treg depletion induces T-cell infiltration and rejection of large tumors. Eur. J. Immunol. 40, 3325–3335. [PubMed: 21072887]

Liao Y, Smyth GK, and Shi W. (2013). The Subread aligner: fast, accurate and scalable read mapping by seed-and-vote. Nucleic Acids Res. 41, e108. [PubMed: 23558742]

Liu C, Chikina M, Deshpande R, Menk AV, Wang T, Tabib T, Brunazzi EA, Vignali KM, Sun M, Stolz DB, et al. (2019). Treg Cells Promote the SREBP1-Dependent Metabolic Fitness of Tumor-Promoting Macrophages via Repression of CD8(+) T Cell-Derived Interferon-gamma. Immunity 51, 381–397.e6. [PubMed: 31350177]

Love MI, Huber W, and Anders S. (2014). Moderated estimation of fold change and dispersion for RNA-seq data with DESeq2. Genome Biol. 15, 550. [PubMed: 25516281]

Luen S, Virassamy B, Savas P, Salgado R, and Loi S. (2016). The genomic landscape of breast cancer and its interaction with host immunity. Breast 29, 241–250. [PubMed: 27481651]

Miller LD, Chou JA, Black MA, Print C, Chifman J, Alistar A, Putti T, Zhou X, Bedognetti D, Hendrickx W, et al. (2016). Immunogenic Subtypes of Breast Cancer Delineated by Gene Classifiers of Immune Responsiveness. Cancer Immunol. Res. 4, 600–610. [PubMed: 27197066]

Nagalla S, Chou JW, Willingham MC, Ruiz J, Vaughn JP, Dubey P, Lash TL, Hamilton-Dutoit SJ, Bergh J, Sotiriou C, et al. (2013). Interactions between immunity, proliferation and molecular subtype in breast cancer prognosis. Genome Biol. 14, R34. [PubMed: 23618380]

Nolan E, Savas P, Policheni AN, Darcy PK, Vaillant F, Mintoff CP, Dushyanthen S, Mansour M, Pang JB, Fox SB, et al.; Kathleen Cuningham Foundation Consortium for Research into Familial Breast Cancer (kConFab) (2017). Combined immune checkpoint blockade as a therapeutic strategy for BRCA1-mutated breast cancer. Sci. Transl. Med. 9, eaal4922.

Noy R, and Pollard JW (2014). Tumor-associated macrophages: from mechanisms to therapy. Immunity 41, 49–61. [PubMed: 25035953]

Osborne CK, Yochmowitz MG, Knight WA 3rd, and McGuire WL (1980). The value of estrogen and progesterone receptors in the treatment of breast cancer. Cancer 46 (12, Suppl), 2884–2888. [PubMed: 7448733]

Panduro M, Benoist C, and Mathis D. (2018). T_{reg} cells limit IFN-γ production to control macrophage accrual and phenotype during skeletal muscle regeneration. Proc. Natl. Acad. Sci. USA 115, E2585–E2593. [PubMed: 29476012]

Parker BS, Rautela J, and Hertzog PJ (2016). Antitumour actions of interferons: implications for cancer therapy. Nat. Rev. Cancer 16, 131–144. [PubMed: 26911188]

Pommier A, Audemard A, Durand A, Lengagne R, Delpoux A, Martin B, Douguet L, Le Campion A, Kato M, Avril MF, et al. (2013). Inflammatory monocytes are potent antitumor effectors controlled by regulatory CD4+ T cells. Proc. Natl. Acad. Sci. USA 110, 13085–13090. [PubMed: 23878221]

Ponomarev V, Doubrovin M, Serganova I, Vider J, Shavrin A, Beresten T, Ivanova A, Ageyeva L, Tourkova V, et al. (2004). A novel triple-modality reporter gene for whole-body fluorescent, bioluminescent, and nuclear noninvasive imaging. Eur J Nucl Med Mol Imaging 31, 740–751. [PubMed: 15014901]

Qian BZ, and Pollard JW (2010). Macrophage diversity enhances tumor progression and metastasis. Cell 141, 39–51. [PubMed: 20371344]

R Development Core Team (2017). R: A language and environment for statistical computing (R Foundation for Statistical Computing).

Ruffell B, and Coussens LM (2015). Macrophages and therapeutic resistance in cancer. Cancer Cell 27, 462–472. [PubMed: 25858805]

Ruffell B, Affara NI, and Coussens LM (2012). Differential macrophage programming in the tumor microenvironment. Trends Immunol. 33, 119–126. [PubMed: 22277903]

Rutkowski MR, Stephen TL, Svoronos N, Allegrezza MJ, Tesone AJ, Perales-Puchalt A, Brencicova E, Escovar-Fadul X, Nguyen JM, Cadungog MG, et al. (2015). Microbially driven TLR5-

dependent signaling governs distal malignant progression through tumor-promoting inflammation. Cancer Cell 27, 27–40. [PubMed: 25533336]

Shi C, and Pamer EG (2011). Monocyte recruitment during infection and inflammation. Nat. Rev. Immunol. 11, 762–774. [PubMed: 21984070]

Shields CWT, Evans MA, Wang LL, Baugh N, Iyer S, Wu D, Zhao Z, Pusuluri A, Ukidve A, Pan DC, and Mitragotri S. (2020). Cellular backpacks for macrophage immunotherapy. Sci. Adv. 6, eaaz6579.

Shimizu J, Yamazaki S, and Sakaguchi S. (1999). Induction of tumor immunity by removing CD25+CD4+ T cells: a common basis between tumor immunity and autoimmunity. J. Immunol. 163, 5211–5218. [PubMed: 10553041]

Spranger S, Bao R, and Gajewski TF (2015). Melanoma-intrinsic β-catenin signalling prevents anti-tumour immunity. Nature 523, 231–235. [PubMed: 25970248]

Sugiura K, and Stock CC (1952). Studies in a tumor spectrum. I. Comparison of the action of methylbis (2-chloroethyl)amine and 3-bis(2-chloroethyl) aminomethyl-4-methoxymethyl −5-hydroxy-6-methylpyridine on the growth of a variety of mouse and rat tumors. Cancer 5, 382–402. [PubMed: 14905426]

Tanaka A, and Sakaguchi S. (2017). Regulatory T cells in cancer immunotherapy. Cell Res. 27, 109–118. [PubMed: 27995907]

Teng MW, Ngiow SF, von Scheidt B, McLaughlin N, Sparwasser T, and Smyth MJ (2010). Conditional regulatory T-cell depletion releases adaptive immunity preventing carcinogenesis and suppressing established tumor growth. Cancer Res. 70, 7800–7809. [PubMed: 20924111]

The Cancer Genome Atlas Network (2012). Comprehensive molecular portraits of human breast tumours. Nature 490, 61–70. [PubMed: 23000897]

Therneau TM, and Grambsch PM (2010). Modeling Survival Data: Extending the Cox Model (Springer).

Thorsson V, Gibbs DL, Brown SD, Wolf D, Bortone DS, Ou Yang TH, Porta-Pardo E, Gao GF, Plaisier CL, et al. (2018). The Immune Landscape of Cancer. Immunity 48, 812–830.e14. [PubMed: 29628290]

Tymoszuk P, Evens H, Marzola V, Wachowicz K, Wasmer MH, Datta S, Muller-Holzner E, Fiegl H, Bock G, van Rooijen N, et al. (2014). In situ proliferation contributes to accumulation of tumor-associated macrophages in spontaneous mammary tumors. Eur. J. Immunol. 44, 2247–2262. [PubMed: 24796276]

Vonderheide RH, Domchek SM, and Clark AS (2017). Immunotherapy for Breast Cancer: What Are We Missing? Clin. Cancer Res. 23, 2640–2646. [PubMed: 28572258]

Wang Q, Hu B, Hu X, Kim H, Squatrito M, Scarpace L, Decarvalho AC, Lyu S, Li P, Li Y, et al. (2017). Tumor Evolution of Glioma-Intrinsic Gene Expression Subtypes Associates with Immunological Changes in the Microenvironment. Cancer Cell 32, 42–56.e6. [PubMed: 28697342]

Wellenstein MD, and de Visser KE (2018). Cancer-Cell-Intrinsic Mechanisms Shaping the Tumor Immune Landscape. Immunity 48, 399–416. [PubMed: 29562192]

Highlights

- Anti-tumor phenotype requires reprogramming of inflammatory monocytes/macrophages
- Myeloid cell functional reprogramming is dependent on IFN-γ produced by CD4T cells
- TAM reprogrammed transcriptome correlates with better prognosis in human cancer

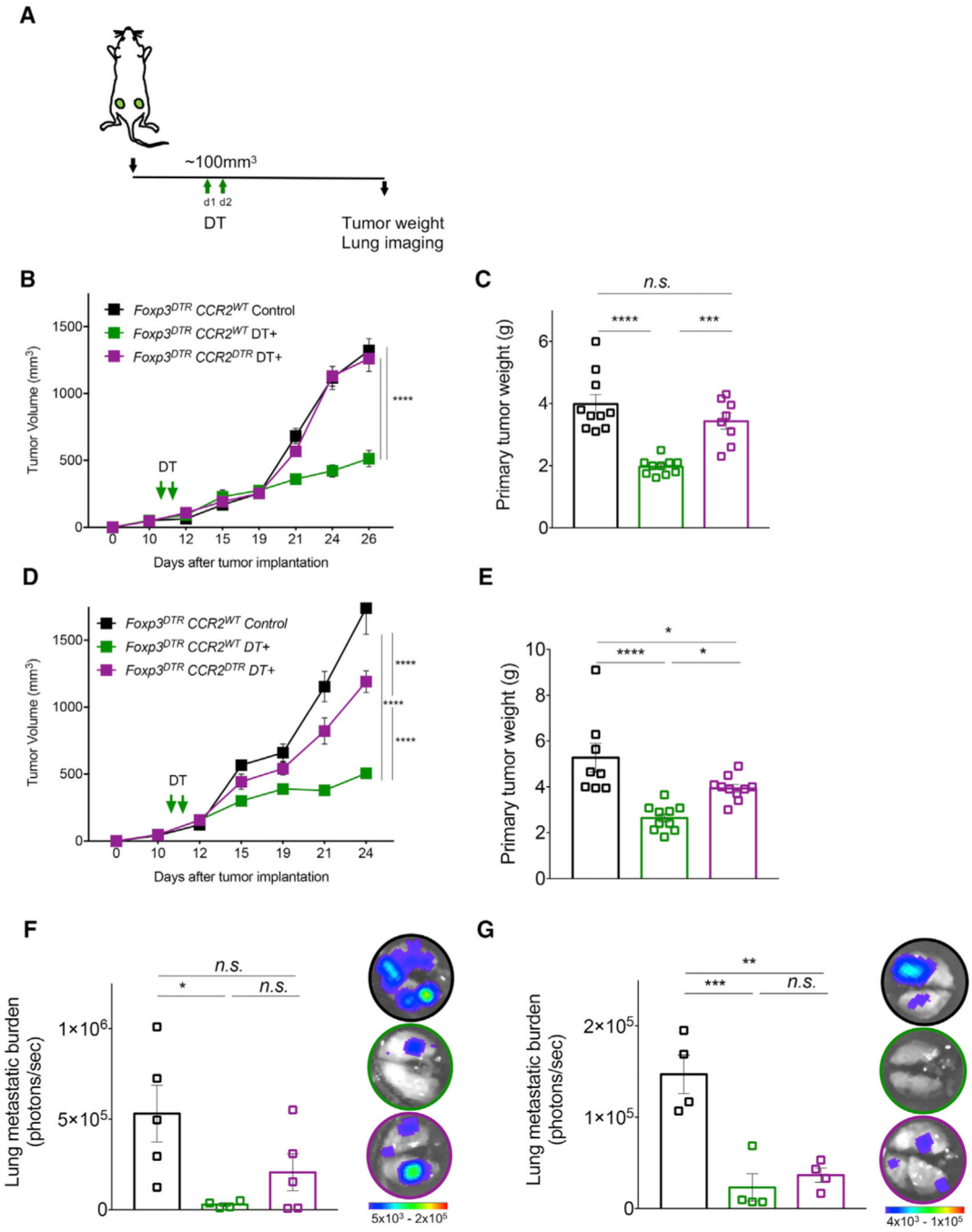

Figure 1. Treg Cell Ablation-Driven Anti-tumor Effects Depend on CCR2-Mediated Recruitment of Bone Marrow Cells

(A) Experimental schematic. Green arrows indicate timing of DT injection. Black arrow indicates endpoint.

(B) Orthotopic tumor growth kinetics of luciferase-transduced PyMT cells injected bilaterally into the fourth mammary gland of the indicated mouse groups; n = 4– 5 mice per group.

(C) Tumor weights obtained at endpoint of experiment (B); n = 8–10 tumors per group.

(D) Orthotopic tumor growth kinetics of luciferase-transduced EO771 cells injected bilaterally into the fourth mammary gland of the indicated mouse groups; n = 5 mice per group.
(E) Tumor weights obtained at endpoint of experiment (D); n = 8–10 tumors per group.
(F) PyMT lung metastatic burden measured by ex vivo bioluminescence at endpoint of experiment (B), with representative images; n = 4–5 per group.
(G) EO771 lung metastatic burden measured by ex vivo bioluminescence at endpoint of experiment (D), with representative images; n = 4 per group.
Each symbol (B–G) represents a single tumor or lung, and data are displayed as means ± SEMs. All individual values are shown. *$p < 0.05$, **$p < 0.01$, ***$p < 0.001$, and ****$p < 0.0001$. Statistical analysis was done by 2-way analysis of variance (B and D) and 1-way analysis of variance (C and E–G) with Tukey's multiple comparison post hoc analysis. Data shown are representative of 2 independent experiments with similar results.

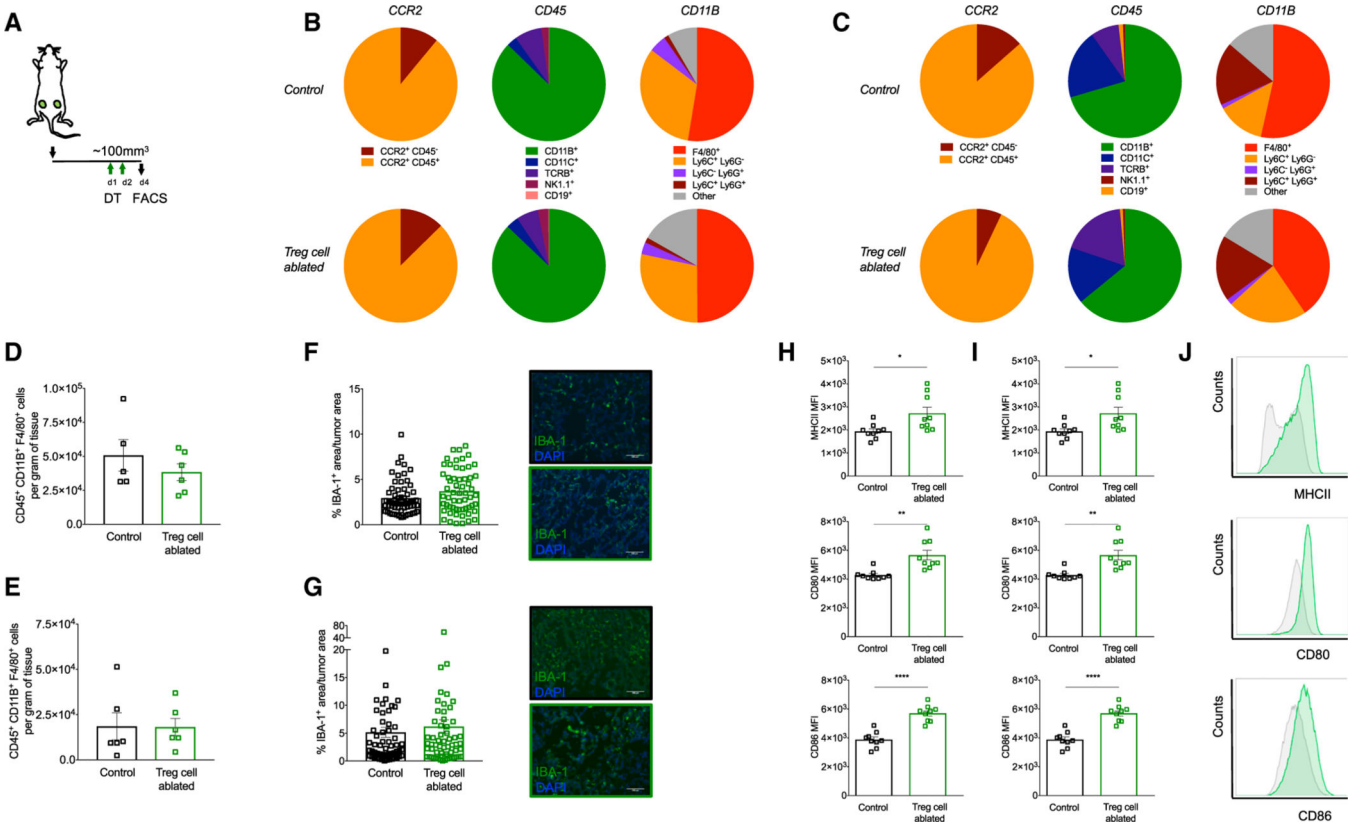

Figure 2. Treg Cell Ablation Alters the Activation State of Tumor-Associated Macrophages (TAMs), but Does Not Affect Their Numbers

(A) Experimental schematic. Green arrows indicate timing of DT injection. Black arrow indicates endpoint for flow cytometric analysis.

(B and C) Fate mapping analysis of $CCR2^+$ cells infiltrating PyMT (B) or EO771 (C) primary tumors orthotopically implanted in *Foxp3*^{DTR} mice untreated (n = 3) or treated with DT (n = 3) 4 days after Treg cell ablation.

(D and E) Flow cytometric quantification of $CD45^+CD11B^+$ $F4/80^+$ cells in PyMT (D) and EO771 (E) primary tumors growing in control or Treg cell ablated mice, performed 4 days post-DT injection; n = 5–6 mice per group for each model.

(F and G) Immunofluorescence quantification of Iba-1-expressing cells in PyMT (F) and EO771 (G) primary tumors growing in control or Treg cell ablated mice, performed 4 days post-DT injection; n = 3 mice per group for each model, 20–22 high-magnification images per mouse.

(H and I) Flow cytometric analysis of macrophage activation markers MHCII, CD80, and CD86, respectively, on $CD11B^+$ $F4/80^+$ tumor-infiltrating macrophages isolated from PyMT (H) or EO771 (I) tumors 4 days after DT treatment.

(J) Representative histogram from (I).

Each symbol represents a single sample, and data are represented as means ± SEMs. *p < 0.05, **p < 0.01, ***p < 0.001, ****p < 0.0001. Statistical analysis was done by 2-tailed unpaired Student's t test (D–I). Data shown are representative of 3 independent experiments (B, H, and I) or 2 independent experiments (C–G) with similar results.

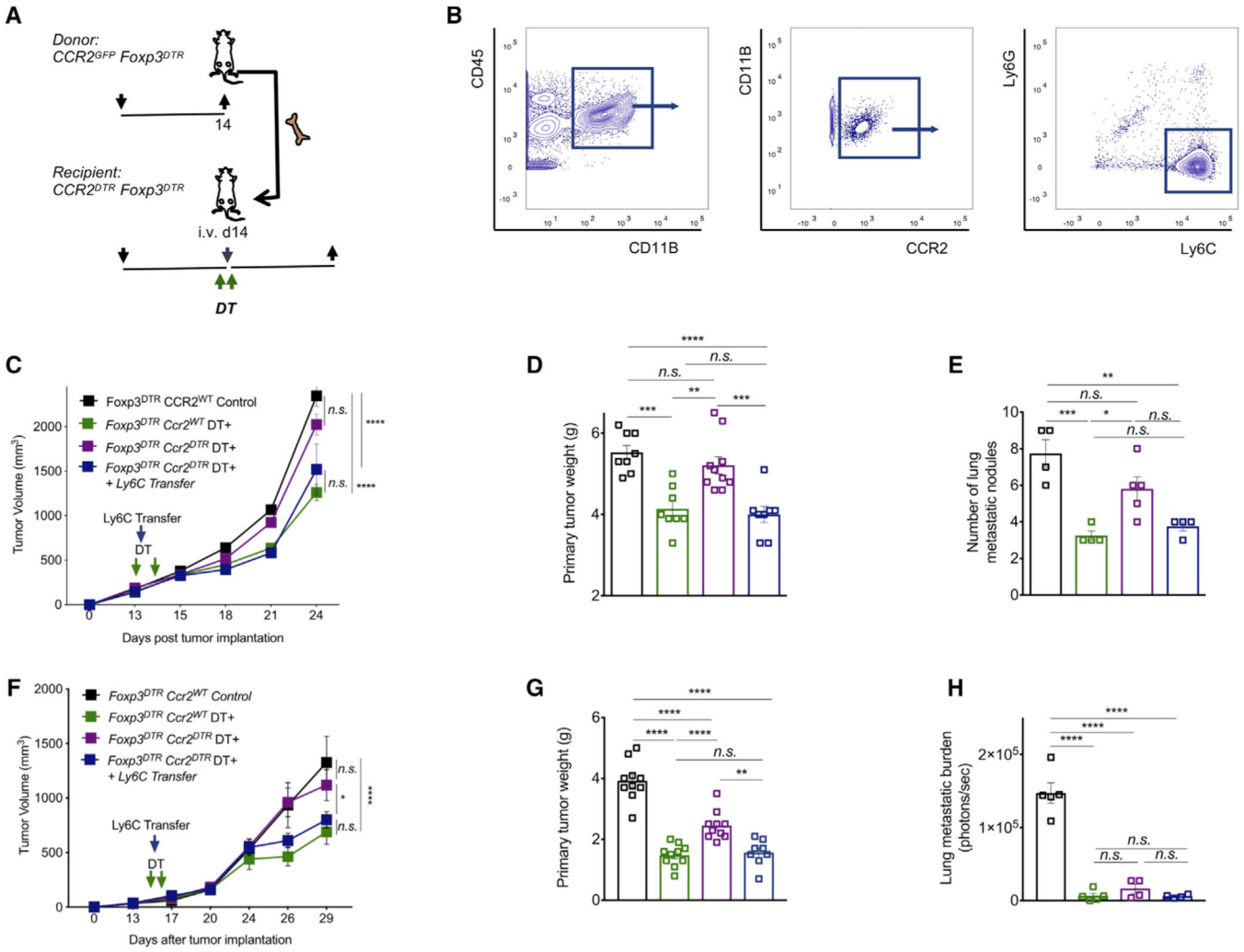

Figure 3. CCR2$^+$ Bone-Marrow-Derived CD11B$^+$ Ly6G$^-$ Ly6C$^+$ Monocytes Are Key Mediators of the Protective Effect after Treg Cell Ablation

(A) Schematic of experimental design. A total of 250,000 CCR2$^+$ CD11B$^+$ Ly6C$^+$ Ly6G$^-$ cells were harvested from the bone marrow of tumor-bearing mice and injected intravenously (i.v.) into the recipient tumor-bearing mice 6 h after initial DT injection. Black arrow indicates tumor cell injection (↓) or endpoint (↑). Green arrows indicate timing of DT injection. Blue arrow indicates adoptive transfer.

(B) Sorting strategy used to harvest inflammatory monocytes from the bone marrow of donor mice.

(C–E) Tumor growth kinetics (C), tumor weight at endpoint (D), and lung metastatic burden (E) for orthotopic PyMT tumors growing in the indicated hosts; n = 4–6 animals per group. Lung metastatic burden was measured by counting tumor nodules under low-magnification, stereoscopic microscopy.

(F–H) Tumor growth kinetics (F), tumor weight at endpoint (G), and lung metastatic burden (H) for orthotopic luciferase-transduced E0771 tumors growing in the indicated host; n = 3–4 animals per group. Lung metastatic burden was determined by *ex vivo* bioluminescence. Each symbol represents a single sample, and data are displayed as means ± SEMs. *p <

0.05, **p < 0.01, ***p < 0.001, and ****p < 0.0001. Statistical analysis was performed by 2-way analysis of variance (C and F, tumor growth curves) and 1-way analysis of variance (D, E, G, and H, tumor weight and lung metastatic burden), followed by Tukey's multiple comparison. Data shown are representative of 2 independent experiments with similar results.

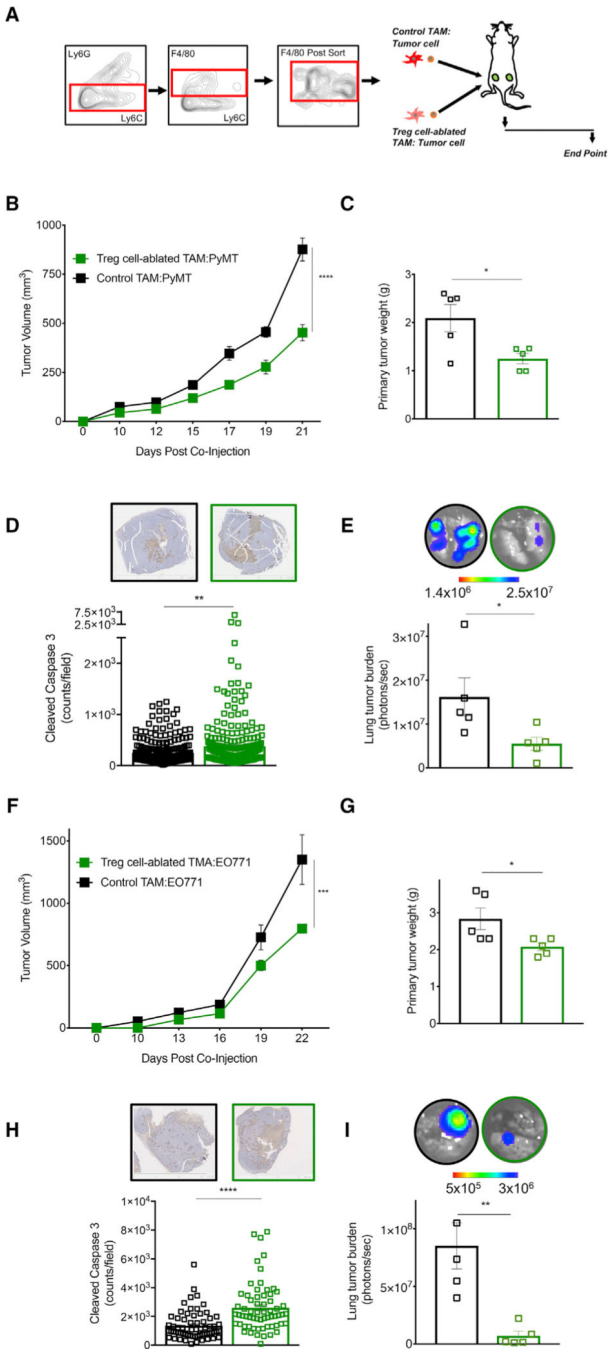

Figure 4. Treg Cell Ablation Induces a Functional Reprogramming of TAMs

(A) Experimental schematic of TAM sorting strategy and co-injection with tumor cells.

(B, C, E) Tumor growth kinetics (B), tumor weight at endpoint (C), and lung metastatic burden (E) after co-injection of TAMs from control or Treg cell ablated tumors with luciferase-transduced PyMT cells; n = 5 mice per group.

(D) Quantification of cleaved-caspase 3 immunohistochemical staining of endpoint tumors from experiment shown in (B), with representative low-magnification images of entire tumors; n = 5 mice each, n = 243–279 high-magnification images per group.

(F, G, I) Tumor growth kinetics (F), tumor weight at endpoint (G), and lung metastatic burden (I) after co-injection of TAMs from control or Treg cell ablated tumors with luciferase-transduced EO771 cells.

(H) Quantification of cleaved-caspase 3 immunohistochemical staining of endpoint tumors from experiment shown in (F), with representative low-magnification images; n = 5 mice each, n = 63– 65 high-magnification images per group. Each symbol represents a single sample, and data are displayed as means ± SEMs. *$p < 0.05$, **$p < 0.01$, ***$p < 0.001$, and ****$p < 0.0001$. Statistical analysis was performed by 2-way analysis of variance with Sidak's multiple comparison test (B and F) and 2-tailed Student's t test (C–E and G– I). Data shown are representative of 3 individual experiments with similar results.

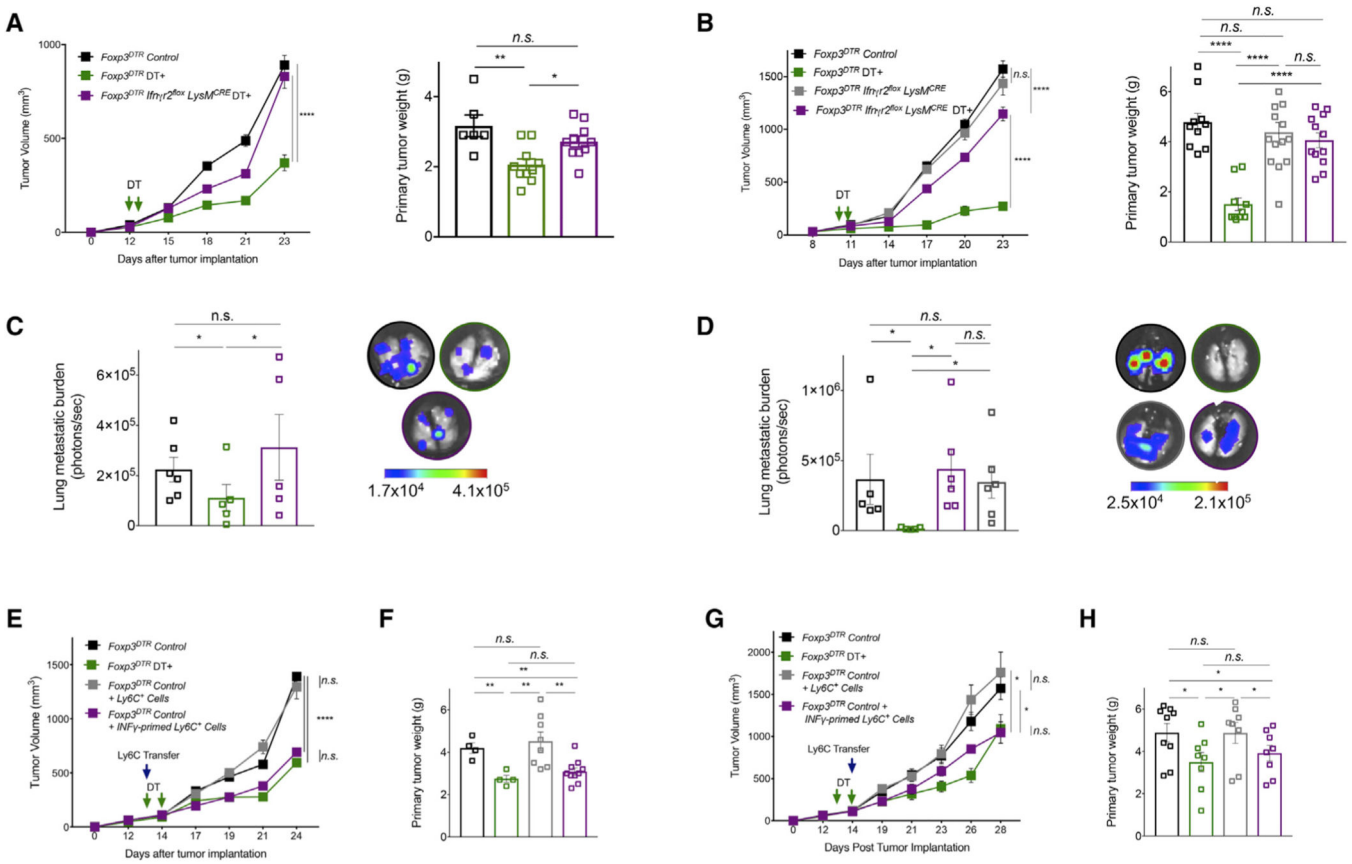

Figure 5. TAM Functional Reprogramming upon Treg Cell Ablation Is Dependent on IFN-γ Signaling

(A) Tumor growth kinetics and endpoint tumor weights of orthotopically injected PyMT cells into indicated animal groups; n = 5–6 animals per group.

(B) Tumor growth kinetics and endpoint tumor weights of orthotopically injected E0771 cells into indicated mouse groups; n = 5–6 animals.

(C and D) Lung metastatic burden determined by ex vivo bioluminescence

(E) Tumor growth and endpoint tumor weight of orthotopically injected PyMT into indicated groups. Bone marrow Ly6C$^+$ cells were mock treated or primed with IFN-γ (100 U/mL) for 30 min before adoptive transfer; n = 3–5 animals per group.

(G and H) Tumor growth and endpoint tumor weight, of orthotopically injected E0771 cells injected into indicated groups. Bone marrow Ly6C$^+$ cells were mock treated or primed with IFN-γ (100 U/mL) for 30 min before adoptive transfer; n = 3–5 animals per group. Each symbol represents a single sample, and data are displayed as means ± SEMs. *p < 0.05, **p < 0.01, ***p < 0.001, and ****p < 0.0001. Two-way analysis of variance with Tukey's multiple comparisons post hoc test (A, B, E, and G), 1-way analysis of variance with Tukey's multiple comparisons post hoc test (A and B, right panels), and 1-tailed Student's t tests (C, D, F, and H). Data shown are representative of 2 independent experiments with similar data.

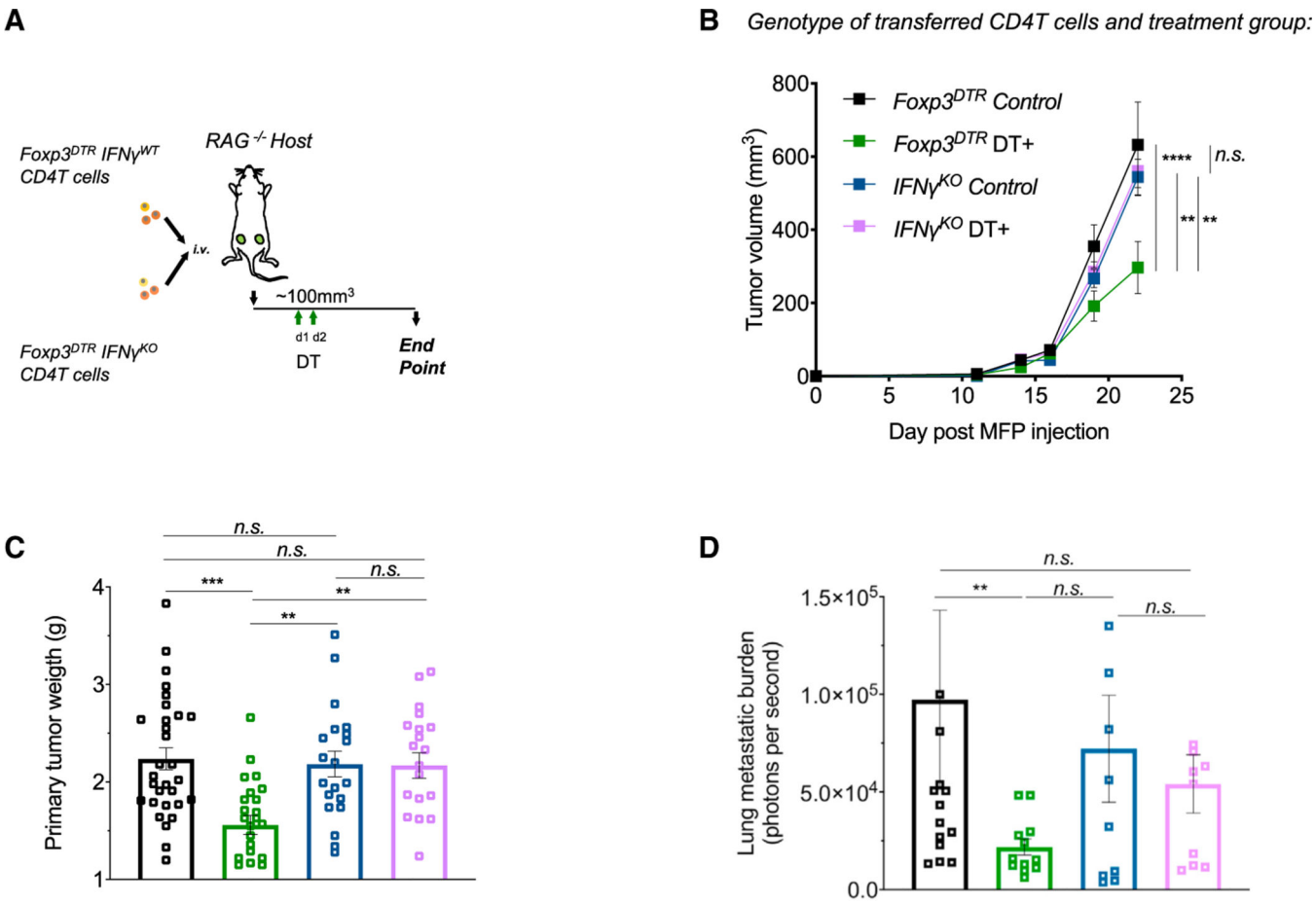

Figure 6. IFN-γ Production by CD4$^+$ T Cells Is Required for Treg Cell Ablation-Dependent Anti-tumor Effect

(A) Experimental schematic of CD4$^+$ T transfer, tumor implantation, and Treg cell ablation.

(B) Tumor growth kinetics.

(C) Endpoint tumor weight.

(D) Lung metastatic burden of orthotopically implanted PyMT tumor cells; n = 10–15 animals per group, pool of 2 independent experiments.

Each symbol represents 1 tumor or lung, and data are displayed as means ± SEMs. **p < 0.01, ***p < 0.001, and ****p < 0.0001. Two-way (B) and 1-way (C) analysis of variance with Tukey's multiple comparisons post hoc test. (D) Mann-Whitney 2-tailed t test.

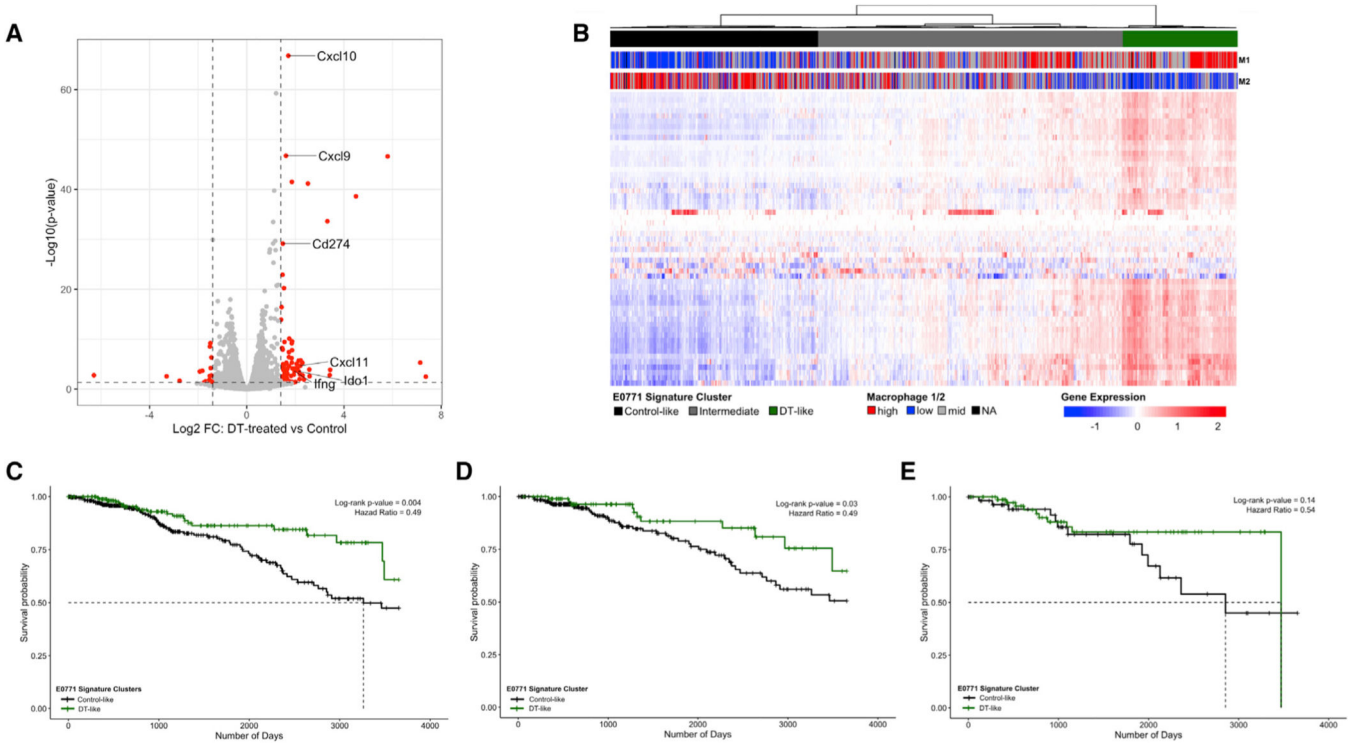

Figure 7. Gene Expression Changes Driven by Treg Cell Ablation in TAMs Are Predictive of Better Prognosis in Human Breast Cancer

(A) Volcano plot of transcriptomic differences between TAMs isolated from control and Treg cell-ablated EO771 mammary tumors. Average of duplicates (Tregcell ablated samples) or triplicates (control samples). Gray indicates no significant change, and red indicates changes above the threshold used for analysis.

(B) Heatmap of human TCGA breast cancer sample gene expression for the human orthologs of the upregulated genes in the mouse-derived signature, clustered using Euclidean distance and Ward linkage using aheatmap() function from the NMF package in R. Green indicates cluster of samples with DT-like gene expression profiles, black indicates cluster of samples with control-like gene expression profiles, and gray indicates samples with intermediate gene expression profiles. M1 and M2 signatures for each TCGA patient (as described in Method Details), with red, blue, and gray indicating a high, low, and intermediate relative signature value, respectively.

(C) Survival analysis of the DT-like and control-like patient groups using the upregulated genes in the whole cohort of breast cancer samples; p = 0.004, hazardratio (HR) = 0.49.

(D) Survival analysis of the DT-like and control-like patient groups in the ER^+ patient population, n = 761; p = 0.03, HR = 0.49.

(E) Survival analysis of the DT-like and control-like patient groups in the ER patient population, n = 231; p = 0.14, HR = 0.54.

KEY RESOURCES TABLE

REAGENT or RESOURCE	SOURCE	IDENTIFIER
Antibodies		
Anti-CD11B	Thermofisher	Cat# 47–0112-82, clone M1/70; RRID: AB_1603193
Anti-Ly6C	Thermofisher	Cat# 25–5932-82, clone HK1.4; RRID: AB_2573503
Anti-Ly6G	Thermofisher	Cat# 61–9668-82, clone, 1A8; RRID: AB_2574679
Anti-F4/80	Thermofisher	Cat# 17–4801-80, clone BM8; RRID: AB_2784647
Anti-CD45	BD Bioscience	Cat# 564279; RRID: AB_2651134
Ghost Violet Viability	Tonbo Bioscience	Cat# 13–0870-T500
Anti-CD11B	Thermofisher	Cat# 47–0112-82; RRID: AB_1603193
Anti-CD4	Tonbo Bioscience	Cat# 50–0042; RRID: AB_2621737
Anti-CD8a	Tonbo Bioscience	Cat# 25–0081; RRID: AB_2621623
Anti-CD19	Tonbo Bioscience	Cat# 50–0193; RRID: AB_2621752
Anti-CD11c	BD Bioscience	Cat# 563048; RRID: AB_2734778
Anti-NK1.1	Tonbo Bioscience	Cat# 20–5941; RRID: AB_2621611
Anti-MHCII	Tonbo Bioscience	Cat# 50–5321; RRID: AB_2621796
Anti-CD86	BD Bioscience	Cat# 564198, clone GL1; RRID: AB_2738663
Anti-CD80	BD Bioscience	Cat# 561955, clone 16–10A1; RRID: AB_10892805
Anti-FoxP3	Invitrogen	Cat# 48–5773-82; RRID: AB_1518812
Cleaved Caspase 3	Cell Signaling Technologies	Cat# 9661; RRID: AB_2341188
Anti-phospho-histone 3 (Ser10)	Millipore	Cat# 06–570; RRID: AB_310177
Iba-1	WAKO	Cat# 019–19741; RRID: AB_839504
F4/80	AbCam	Cat# ab6640; RRID: AB_1140040
Bacterial and Virus Strains		
pLVX-Puro Vector	Clonetech/Takarabio	Cat# 632164
thymidine kinase 1, GFP and firefly luciferase (TGL vector)	Ponomarev et al., 2004	n/a
Chemicals Peptides and Recombinant Proteins		
Liberase TL	Sigma	Cat# 5401020001
Diphtheria Toxin, Unnicked, from Corynebacterium diphtheriae	List Biological Laboratories	Cat# 150
Mouse IFN-γ (Carrier Free) RPx-Pro	Tonbo	Cat# 21–8311
Deposited Data		
RNASequencing data from tumor-associated macrophages isolated from EO771 mammary tumors	This paper	GSE159806
Experimental Models: Cell Lines		
PyMT	Bos et al., 2013	n/a
E0771	CH3 BioSystems	RRID:CVCL_GR23

REAGENT or RESOURCE	SOURCE	IDENTIFIER
BRPKP110	Rutkowski et al., 2015	n/a
Experimental Models: Organisms/Strains		
MMTV-PyMT C57/BL6	Franklin et al., 2014	n/a
B6.129(Cg)-Foxp3tm3(DTR/GFP)Ayr/JMus musculus	The Jackson Laboratory	Stock No: 016958
Ccr2 reporter (*Ccr2^{GFP}*)	Hohl et al., 2009	n/a
Ccr2 depleter (*Ccr2$^{DTR-CFP}$*)	Hohl et al., 2009	n/a
Ifngr2^{flox}	Lee et al., 2015	n/a
B6.129P2-*Lyz2$^{tm1(cre)Ifo}$*/J	The Jackson Laboratory	Stock No: 004781
B6.129S7-*Ifng^{tm1Ts}*/J	The Jackson Laboratory	Stock No: 002287
NOD-scidIL2Rgamma^{null}	The Jackson Laboratory	Stock No: 005557
Software and Algorithms		
GraphPad Prism	GraphPad Prism	RRID:SCR_002798
FlowJo	FlowJo	RRID:SCR_008520
ImageJ	ImageJ	RRID:SCR_003070
FastQC v.0.11.5	Andrews, 2010	https://www.bioinformatics.babraham.ac.uk/projects/fastqc/
Trimmomatic v.0.33	Bolger et al., 2014	http://www.usadellab.org/cms/?page=trimmomatic
Subread v1.6.2	Liao et al., 2013	http://subread.sourceforge.net/
R v.3.4.0	R Development Core Team, 2017	https://www.r-project.org/
NMF R package v.0.22.0	Gaujoux and Seioghe, 2010	https://cran.r-project.org/web/packages/NMF/index.html
DESeq2 R package v.1.16.1	Love et al., 2014	https://bioconductor.org/packages/release/bioc/html/DESeq2.html
TCGABiolinks v2.5.9	Colaprico et al., 2016	https://bioconductor.org/packages/release/bioc/html/TCGAbiolinks.html
UCSF's OrthoRetriever	UCSF	http://lighthouse.ucsf.edu/orthoretriever/
National Cancer Institute's Genomic Data Commons (GDC) Data Portal	Grossman et al., 2016	https://portal.gdc.cancer.gov/
survival R package v2.42–6	Therneau and Grambsch, 2010	https://cran.r-project.org/web/packages/survival/index.html
survminer R package v0.4.2	Kassambara et al., 2018	https://cran.r-project.org/web/packages/survminer/index.html
Other		
TCGA BRCA dataset	The Cancer Genome Atlas Network, 2012	TCGA-BRCA